UNIVERSITY OF OKLAHOMA

GRADUATE COLLEGE

# A LOW-FREQUENCY ASYMPTOTIC FORMULATION TO ESTIMATE HYDRAULIC FRACTURE PROPERTIES FROM PRESSURE DATA

A THESIS

SUBMITTED TO THE GRADUATE FACULTY

in partial fulfillment of the requirements for the

Degree of

MASTER OF SCIENCE

By

RAFEEF AL-SAMMARRAIE
Norman, Oklahoma
2016

A LOW-FREQUENCY ASYMPTOTIC FORMULATION TO ESTIMATE HYDRAULIC FRACTURE PROPERTIES FROM PRESSURE DATA

A THESIS APPROVED FOR THE
MEWBOURNE SCHOOL OF PETROLEUM AND GEOLOGICAL ENGINEERING

BY

_____
Dr. Deepak Devegowda, Chair

_____
Dr. Siddharth Misra

_____
Dr. Rouzbeh Moghanloo

# DEDICATION

This thesis is dedicated to my parents

Namuq Al-Sammarraie and Ma'arb Hussein

for their endless love, support, and encouragement.

## ACKNOWLEDGEMENTS

First and foremost, I would like to extend my heartfelt gratitude to my loving parents, whose good example has pushed me to accomplish all I aspire to achieve. Thank you.

I owe so much to my entire family and friends for their endless support and their absolute belief that I can achieve so much. I cannot thank you enough for you sincere love and help without which I would not have been able to accomplish this thesis. I want you to know that you count so much.

Finally, I would like to dedicate this work to the people who kept me going when I wanted to give up.

# Table of Contents

# List of Tables

# List of Figures

## Abstract

The key drivers of success in unconventional oil and gas recovery, specifically in shale plays, is the rapid growth in hydraulic fracturing and horizontal well technology. With these completion methods, wells contact increasingly larger reservoir volumes with highly conductive pathways for fluid flow from ultra-low permeability formations.

Although the industry is moving towards larger fracture stage designs and increasing number of fracture stages per well, there is very limited post-fracture analysis of the subsequent well performance. Decline curve analysis and rate/pressure transient analysis are the most common approaches to interpret production data, often in real-time, to assess formation and hydraulic fracture properties such as matrix permeabilities and effective fracture half lengths. While these methods are powerful and have been successfully applied to several thousands of wells across several shale plays, the biggest drawback of these approaches is that they have limited utility when addressing multiphase flow and when dealing with complex fracture patterns. This is because the underlying equations rely on analytic formulations that are restricted to certain classes of well and completion geometries.

In this thesis, I utilize a numerical simulation based approach that addresses the challenges of analytic formulations and simultaneously allows for rapid characterization of the reservoir and the hydraulic fracture geometries. The method is based on utilizing the frequency content of pressure data to estimate large-scale reservoir- and completion-related variables. The

advantage of this approach is that is permits generalization to any level of fracture and well complexity. The numerical simulation model can additionally be constrained to known heterogeneities and structural features and therefore preserves geologic realism for more accurate forecasting and predictions. The approach has previously been applied to cross-well pumping tests for interpretation of inter-well connectivity. In this thesis, I demonstrate the power and utility of this approach on synthetic case studies as well as a field-case study to estimate hydraulic fracture permeabilities/conductivities.

# Chapter 1: Introduction and Background

Hydraulic fracturing is an essential part of well completions in ultra-low permeability shale formations. By hydraulically fracturing the formation, the contact area of the wellbore with the formation is enhanced by several orders of magnitude. This allows for economic production of hydrocarbons from previously uneconomic shale plays. In fact, the significance of hydraulic fracturing to North American hydrocarbon production cannot be minimized. Valko and Economides (1995) indicate that approximately 50% of oil wells and 70% of gas wells were hydraulically fractured in North America since 1950s. Since then with the advent of development activity in shales, this number is likely to be higher.

There are many factors that govern the eventual design of the fracture for a specified well and completion geometry. These factors can be reservoir specific such as in-situ pressure and stresses, reservoir permeability, formation moduli, and fluid viscosity (Rahman and Joarder 2006) or they may be operations-related such as the size of the fracture treatment, the pumping rate, the volume of fracture fluid pumped, the amount of proppant used and the pressure at which the fracture was created.

Economides and Nolte (2000) state that hydraulic fracturing occurs due to an initial rise in pressure that initiates fractures at weak points within the rock or reactivates existing natural fractures. As the injection continues, the fractures continue growing and the rate of growth is dictated by fluid injection and leak-off rates. At injection rates faster than leak off, the increase in

pressure is accompanied by fracture propagation. The initial pressure required to initiate fracture growth is known as the fracture initiation pressure (FIP). However, as the injection stops, the fractures start to close due to the closure stresses as shown in **Fig. 1.** In order to keep the fractures open, the pumping schedule also requires the use of a propping agent. Proppants are usually sand grains or material of similar properties that help keep fractures open as long as possible.

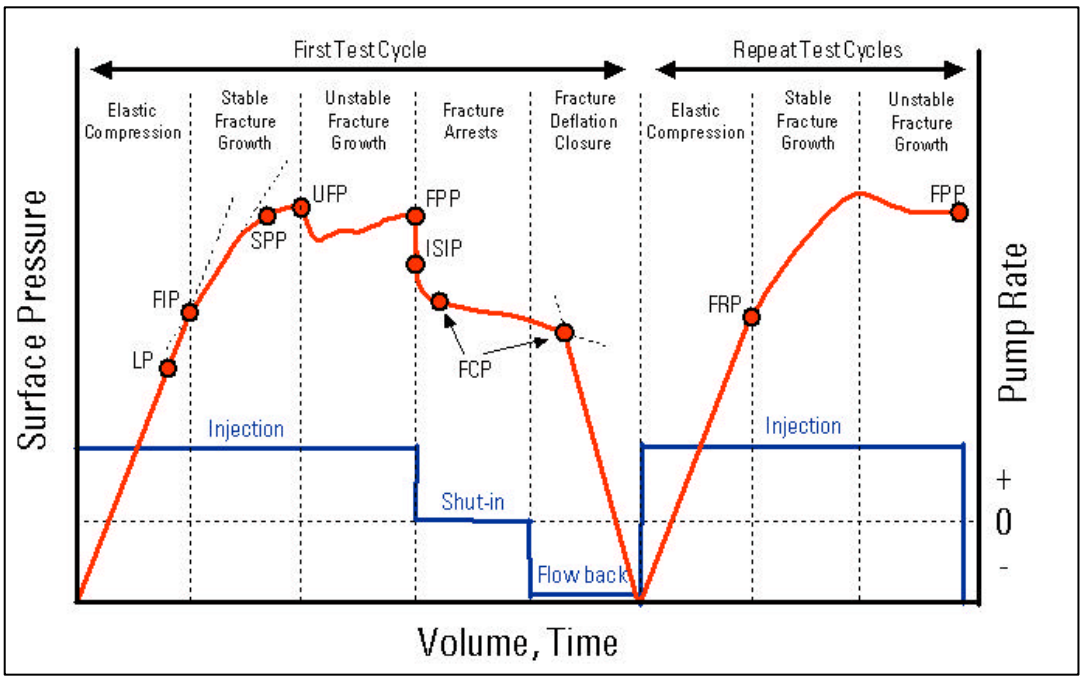


**Figure 1 - The figure shows the pressure trend exhibited with increasing volumes of mud pumped. The formation starts breaking at FIP with increasing injection volume. After the injection is stopped, the fractures initiated start closing at FCP (after Lee et al. 2004).**

The figure above, Fig.1 is a typical pressure-volume/time diagram used to describe the results of a Leak-Off Test (LOT). Usually Leak-Off Tests are carried to evaluate the integrity of the cementing job as well as reservoir formation around the well (Lee et al. 2004). The term LP is the Limit Pressure; FIP is the Fracture Initiation Pressure; SPP is the Stop Pump Pressure. In

addition, UFP is the Unstable Fracture Pressure; FPP is the Fracture Propagation Pressure; and ISIP is the Instantaneous Shut In Pressure. The terms FCP and FRP are the Fracture Closure Pressure and the Fracture Reopening Pressure, respectively.

### 1.1 Hydraulic Fracture

Hydraulic fracturing is what happens to the formation when a fluid is pumped at faster rates than the fluid can spread through the pores of the formation. Pumping fluids at injection pressures higher than formation pressure forces the formation to breakdown as seen in Fig.1. This breakage is called a hydraulic fracture as it is created due to hydraulic fluid pressure. The pressure at which the fracture is initiated is called the Fracture Initiation Pressure. Generally, the fractures are created in the direction perpendicular to the minimum stress.

As the high pressure injection fluid is retained, the fracture propagates at pressures defined as Fracture Propagation Pressures, as shown in Fig.1. This exposes the undamaged formation to the pumped fluid and the increasing pressure which result in more fractures. If fluid pumping is stopped and the injected fluid leaks off, the fractures attempt to close as noticed in Fig.1. The pressures at which the fractures close are called Fracture Closure Pressure. In order to keep the fractures open, a propping agent is used. The propping agent is added to the injection fluid and together they are pumped into the formation.

The injection fluid flows back to the well, while the propping agent remains inside the fractures (API HF1 2009).

The design of the hydraulic fracturing procedure is very complicated. Many parameters are studied and integrated to ensure the success of the process. Rock mechanics, fluid mechanics and fluid chemistry are integral elements of the hydraulic fracture treatment design because they control fracture geometry, fluid flow, leakoff, proppant delivery and long-term proppant performance (Economides and Nolte 2000). In this section, I provide a brief overview of some of the variables that impact fracture design and fracture complexity.

### 1.1.1 In-Situ Stress

Fracture orientation, geometry and direction of propagation are controlled by the in-situ stress field (Smith and Shlyapobersky 2000). This field is defined by three principal compressive stresses, a vertical stress and a maximum and minimum horizontal stresses, which are perpendicular to each other. The minimum in-situ stress is also known as the fracture closure pressure and controls the direction in which fractures grow and propagate.

If the pressure within the fracture is higher than the fracture closure pressure, the fracture remains open. However where the fracture closure pressure is higher than the pressure within the fracture, the fracture inevitably closes.

Hubbert and Willis (1957) conducted experiments on rocks concluding that fracture orientation is controlled by the injection and overburden pressures. Fractures at areas subjected to thrust faulting should be horizontal when the injection pressure is equal or greater than the overburden pressure. However, fractures should grow vertically in areas subjected to normal faulting when the injection pressure is less that the overburden pressure. Also, the pressure created as a difference between the two stressed geological elements dictates the growth length of the fracture. Therefore, the stresses in pay, underlying, and overlying zones must be obtained for accurate hydraulic fracturing procedure.

The value of the minimum stress is extremely important in dictating the direction of fracture formation and growth. The breakdown or fracturing pressure depends greatly on the minimum stress. As mentioned above, hydraulic fractures grow in the direction normal to the minimum stress direction. At locations where the minimum principal stress is in the vertical direction, horizontal fractures form. Vertical fractures form when the vertical stress is the maximum principal stress and the horizontal stress is the least stress (API HF1 2009). Horizontal fractures form parallel to the formation bedding plane while vertical fractures are perpendicular to the bedding plane.

The growth of fractures is controlled by the in-situ stress difference between layers. The in–situ stresses of the overlying and adjacent zones control fracture growth. In addition, the direction of the three principal stresses also influences the geometry and the length of the fracture.

An adequate barrier of fracture migration is characterized by a greater in-situ stress which results in a dominant stress difference. In cases where the overlying zones possess high stress confinements, the upward fracture migration is stopped due to the zone's ability to contain the fluid injection pressure. This ability is characterized by high rock strength and elasticity promoted by the stress confinements. The upward or downward growth of fractures are controlled by the hydrostatic gradient of the injection fluid in comparison to the vertical gradient of the minimum horizontal in-situ stress. In cases where the hydrostatic gradient is less than the minimum horizontal stress, upward or downward propagation is possible (Economides and Nolte 2000).

The propagation of the fractures in any other direction is controlled by the direction of the maximum horizontal stress. If a fracture propagate to another boundary zone where the direction of the principal stress is different, the fracture will attempt to re-orient its growth direction normal to the direction of the minimum stress. This is the reason behind vertical fractures transforming to horizontal fractures when they propagate upward towards zones with minimum stresses in the vertical direction (Simonson et al. 1978).

### 1.1.2 Reservoir Properties

The dimensionless fracture conductivity, $C_{fD}$ is defined as the relationship between the ability of the fracture to carry fluid and the reservoir's ability to supply it with fluids (Pearson 2001). This quantity is

controlled by the reservoir permeability as shown below in Eq. 1. The parameters ( $k_f$ ) and ( $k$ ) are the fracture and matrix permeabilities, respectively. The fracture width is defined by the notation ($w$) while the fracture half-length is defined by the parameter ($k_f$). On the other hand, the conductivity of a fracture is the product of the proppant pack permeability and the fracture width. This conductivity usually decreases with time due to many factors such as propping agent embedment, crushing, and/or stress corrosion.

Generally a value of $C_{fD}$ greater than 50 is considered to represent an infinite conductivity fracture in which the pressure gradient within the fracture can be assumed to be negligible compared to the pressure drop within the matrix.

$$C_{fD} = \frac{k_f w}{k x_f} \tag{1}$$

Because the dimensionless fracture conductivity, $C_{fD}$ is controlled by the matrix permeability that has values on the order of a few to 10s of nanodarcies, the hydraulic fractures in shales are generally considered to be infinite conductivity fractures.

Matrix permeability also influences the amount and rate of leak-off during a hydraulic fracturing operation. The efficacy of a hydraulic fracturing job can be controlled by mitigating excessive leak-off to high permeability regions and natural fractures. This is done to redirect the flow of the injection fluid towards low permeability regions for more fracture initiations. In addition, the importance behind controlling the flow and rate of leak-off lays in

the significant effect of leak-off on the final geometry of the fractures created (Penny et al. 1985). In the next section, I also provide an overview of the rock mechanical properties that control fracture growth and initiation.

### 1.1.3 Rock Mechanics

Because the fracture is initiated by applying fluid pressures in excess of the breakdown strength of the rock, other properties that control fracture growth are related to the mechanical strength of the rock. These include the Young's Modulus and Poisson's ratio (Warpinski et al. 1982). These may be obtained by the use of well log data or by conducting experiments in the lab on retrieved core samples (Economides and Nolte 2000). Young's Modulus defined the stiffness of the formation which affects the fracture geometry. As the value of Young's Modulus increases, the stiffness of the formation increases. High formation stiffness forces the initiated hydraulic fractures to have a narrow width. However, the fracture length growth increases due to high friction pressure gradients created by the narrow widths (Rahim and Holditch 1992).

The brittleness of a rock is defined by the both Young's Modulus and Poisson's ratio. The former describes the formations potential to maintain fracture propagation while the latter indicates the formation ability to fail. A brittle formation, such as Shale, characterized by high Young's Modulus and low Poisson's ratio tend to fail easily (Rickman et al. 2008). In unconventional resources, identifying brittle regions is important for the success of the

hydraulic fracturing process. This is because the high brittleness characteristic of Shales facilitates fracture initiation and propagation.

In cases where the rock mechanical properties are unavailable, there are several mineralogy-based proxies for the brittleness of the formation. One of the first mineralogy-based brittleness index was proposed by Jarvie et al. (2007). These have since been modified to also include the effect of TOC in shales. It is defined as shown below in Eq. 2.

$$\mathrm{BI} = \frac{\mathrm{Qz}}{\mathrm{Qz+Ca+Cly}} \tag{2}$$

The term (BI) is the Brittleness Index; Qz is the fractional Quartz content; Ca and Cly are the fractional Calcite content and the clay content, respectively. Other measures of brittleness have also been developed based on the use of seismic data that provides significantly larger areal and vertical coverage (Alzate and Devegowda 2013 and Perez and Marfurt 2015)

The concept of brittleness is sometimes misleading. A formation can possess high brittleness as well as high rock strength. Rock strength influences the rock's potential to break. This creates the confusion of identifying the best areas to fracture. Therefore, identifying regions characterized by high susceptibility to fracturing is a more adequate method. This approach utilizes the Ultimate Rock Strength of a formation to infer the formation's potential to fail. Formations with high potential to fracture tend to possess low formation strength (Bai 2015).

### 1.1.4 Proppants

After initiation of the fracture and reduction of pump pressures, the fractures may close if the fracture closure pressure exceeds the fluid pressure within the fracture. In order to maintain a high conductivity fluid migration pathway, the fracture treatment includes the use of proppants. Their composition and size depends on the lithology of the formation, the desired long-term well performance and cost (Veatch and Moschovidis 1986). Proppant selection depends on many parameters such as the maximum stress effect on the proppants, conductivity at in-situ conditions, and designed fracture width. In addition, the perforations size, the injected fluid viscosity, and temperature are among many other parameters that determine the selection of proppants' type, size, and concentration.

In order to ensure that the fracturing job is successful, we need to avoid screenout. Screenout occurs when the continued injection of the fluid inside the formation requires additional high pressure and high proppant loadings at the tip of the fractures or perforations (Economides and Nolte 2000). The proppants will create a bridge across the fracture or the perforations which will block flow and plug the well.

Screenout in the fracture occurs when the fluid pumping rate is lower than the fluid loss rate occurring at the fracture tip. In addition, screenout occurs when a propping agent is pumped inside fractures with narrow widths. In both situations, the proppant particles are forced to enter the fractures and solidify restricting flow. In order to ensure that no screenout occurs, the

formation must be flushed by a pad before any proppants are injected. Also, the proppants and the slurries must be pumped at volumes and rates that are consistent with the amount of fluid leakoff (Nolen-Hoeksema 2013).

### 1.2 Post Treatment Evaluation

The effectiveness of the hydraulic fracturing procedure and its impact on well deliverability, its pressure responses and well drainage volumes is a key element of post-treatment fracture evaluation. This is often performed to predict long-term well performance, to estimate optimal well and fracture spacing and to predict the stimulated reservoir volume (SRV) (API HF1 2009).

In unconventional shale plays, the horizontal wells are often completed with multistage hydraulic fracture treatments over the length of the lateral (Gutierrez et al. 2014). Each of these stages is associated with a set of hydraulic factures that increase fracture-fracture, well-fracture, and reservoir-fracture contact as shown in **Fig. 2.** As these contacts are created and enlarged, the stimulated reservoir volume (SRV) is increased. The SRV represents the volume of the reservoir that contains re-activated natural fractures as well as induced fractures that connect to the wellbore.

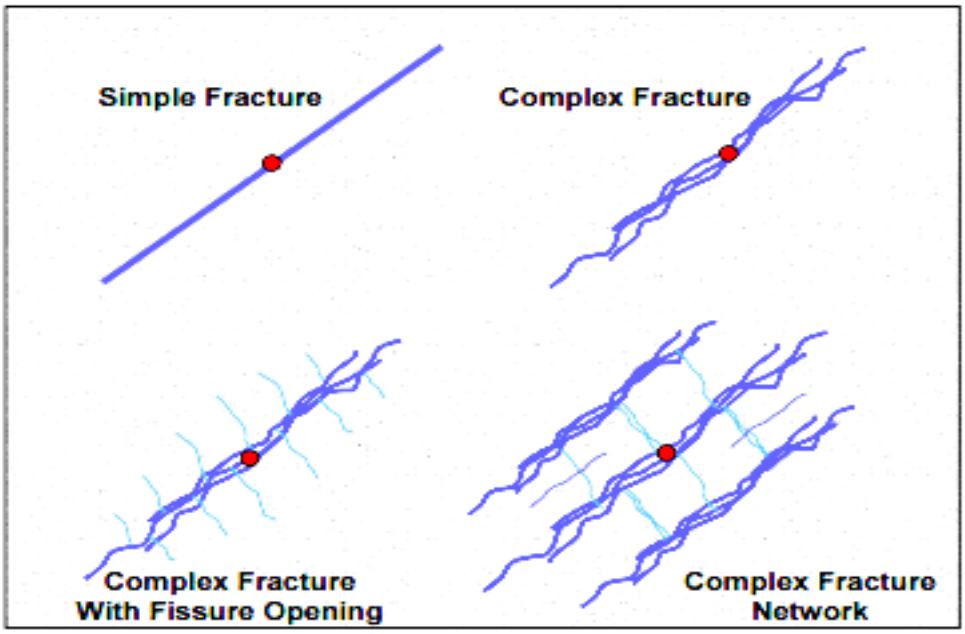


**Figure 2 - The different complexities of fractures (after Mayerhofer et al. 2008)**

The size of the SRV depends greatly on the size of the treatment pumped while fracturing. Higher treatment size generally results in a larger size of SRV which ultimately increases the production rates. In vertical wells, the size of the treatment usually controls the size of SRV. However, in horizontal wells, more factors can be manipulated to increase the stimulated volume. Two other factor affecting SRV are the lateral length and number of stages. Increasing the number of stages and the use of longer laterals enlarges the SRV size but comes at a higher cost and operational complexity. Perforation clusters, diversion technics, and completion systems in addition to many others impact the size of the SRV (Zimmer 2011).

Direct treatment evaluations are usually performed through the use of different logging and fracture-mapping procedures such as microseismic data analysis. Indirect measurements include analysis of the pressure response in

well testing as well as production data analysis (Barree et al. 2002). Indirect methods are capable of probing larger reservoir volumes in comparison to well logs and can provide an estimate of the fracture characteristics at any period while a well is operating. The major limitation of this technique is its strong dependency on the use of assumed models of reservoir formation and fluids characteristics. In this section, I provide a brief overview of some of these post-treatment evaluation methods.

### 1.2.1 Fracture-Mapping and Logging Techniques Evaluation

There are many logging and fracture imaging techniques that are used to evaluate the success of hydraulic fracturing (Bennet et al. 2005). Logging and imaging tools such as caliper and production logging usually generate fair amounts of information about the fracture. They are usually restricted to near wellbore distances due to their small investigation lengths. Far-field measurements such as tiltmeters and microsiesmic imaging provide large scale information about the fractures and the reservoir. Together, the near and far field tools provide well detailed look of the fractures (Barree et al. 2002).

Fracture growth can also be mapped by utilizing temperature surveys. Because the fracturing fluid is initially cooler than the formation temperature the fracture height may be conveniently mapped. While temperature surveys are promising, they are limited to logging runs where the fluid and formation temperatures are sufficiently different. A method of mapping fracture growth and complexity in three-dimensional space for multiple fracture stages is the

use of microseismic imaging. Microseismic imaging relies on mapping shear slippage wave events arising from fracturing (Mayerhofer et al. 2008).

As the formation and natural fractures break due to the high pressures exerted by the injected fluids, shear slippages occur adjacent to the fractures resulting in clouds of microseismic events. These microseismic clouds provide estimates of the locations where the rock has failed. Ultimately, the estimation of the fracture locations, length, height, azimuth, and asymmetry provides enough information to estimate the size of the SRV. Ultimately, the estimation of the stimulated reservoir volume in a three dimensional model showing the fracture networks and the areas that have been affected the stimulation process (Fisher et al. 2004) becomes possible as shown in **Figs. 3 and 4.**

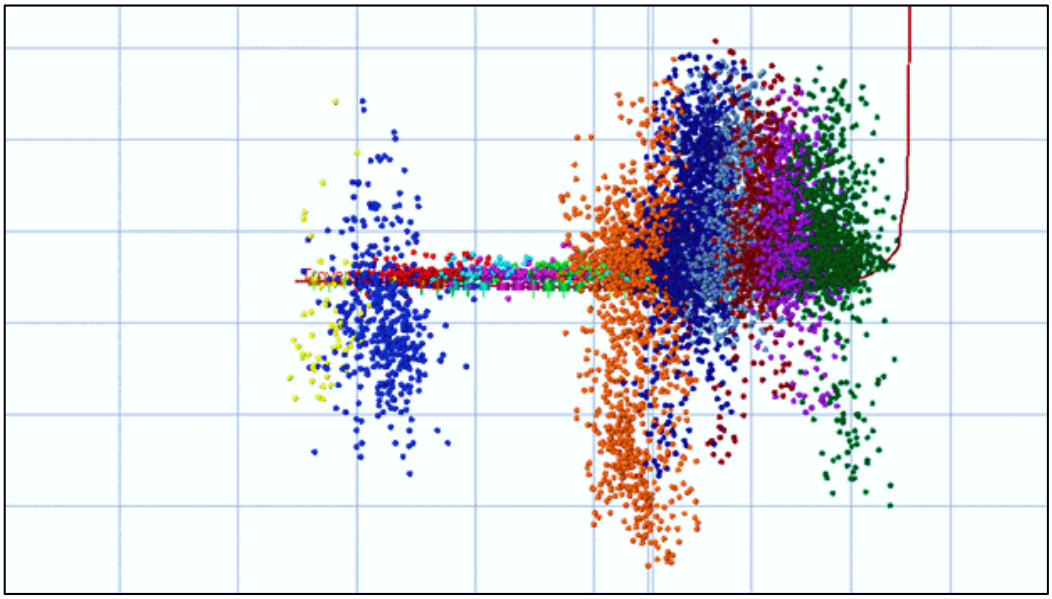

**Figure 3 - An example of Microseismic events (after Lewis and Perry 2011).**

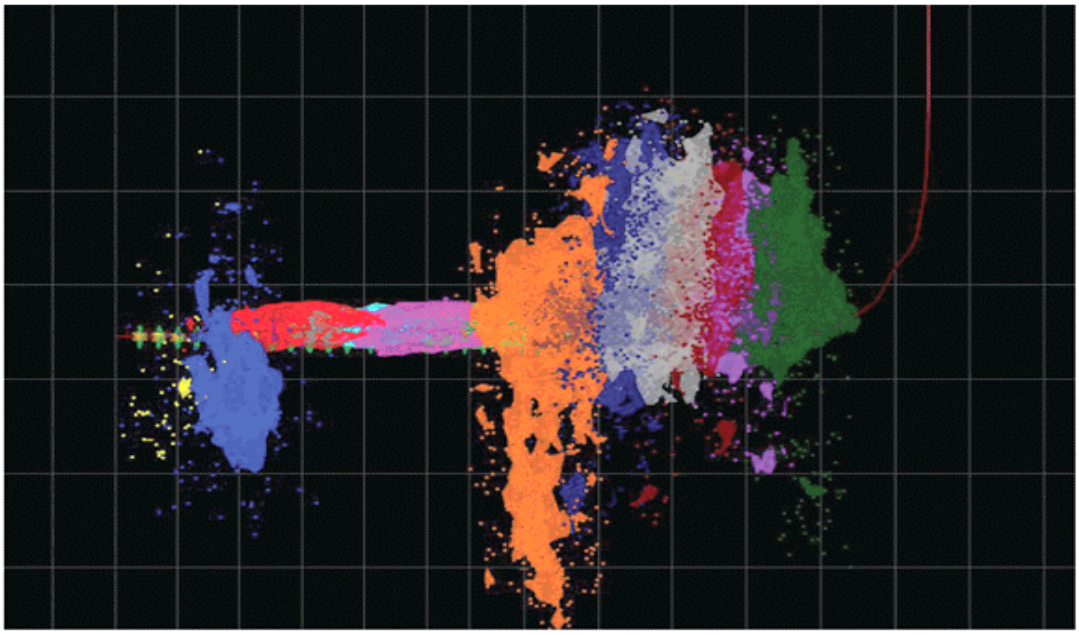

**Figure 4 - An example of SRV Estimation (after Lewis and Perry 2011)**

### 1.2.2 Flow Regimes and Pressure Transient Analysis

Well testing and production data analysis are powerful techniques to evaluate hydraulic fracture geometry. The fractures, their orientation and geometry create conditions for new flow regimes which alter the pressure response within the reservoir (Ozkan et al. 1987).

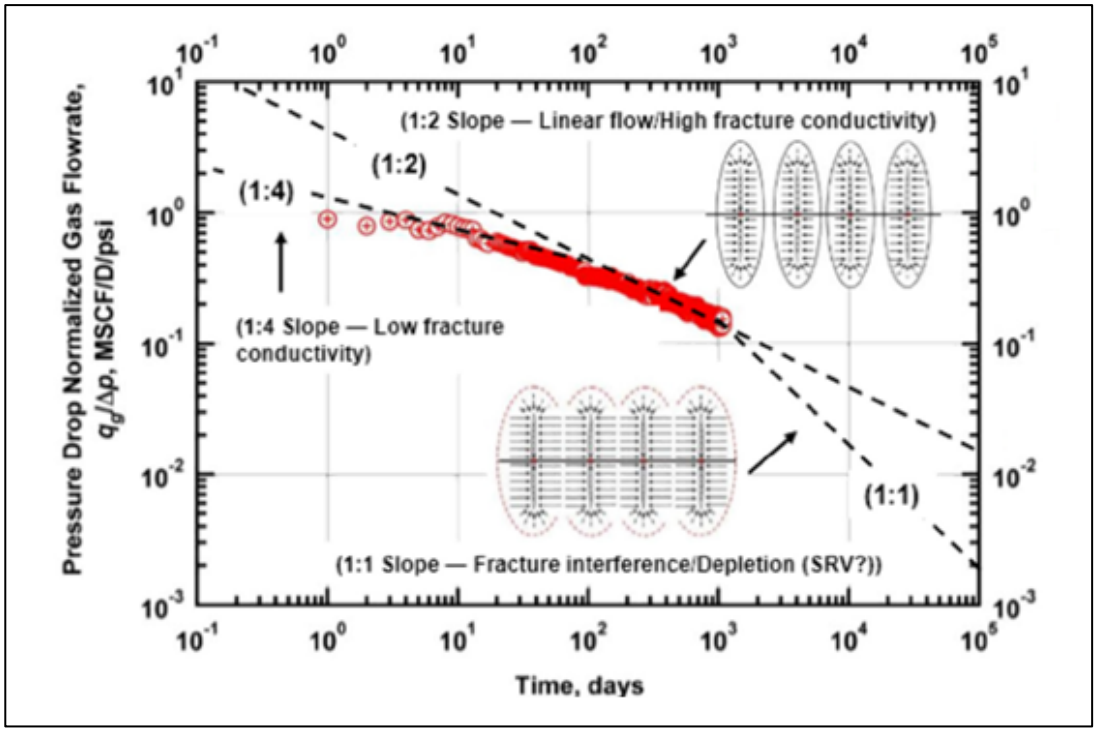


**Figure 5 - Typical diagnostic plot showing expected flow regimes in a multi-fractured horizontal well (after Blasingame 2015)**

The pressure response observed in fractured reservoirs display different flow regimes as shown in **Fig 5.** In hydraulically fractured horizontal wells where the fracture conductivity is finite, a bilinear flow regime is observed. This flow regime is characterized by two linear flows; from matrix to fracture and from the fracture to the well. The second flow regime exhibited by hydraulically fractured horizontal wells is the linear flow regime. This regime occurs when there is a flow towards the fractures of the fractured well. On diagnostic plots, the bilinear flow regime is recognized as a 1:4 slope while the linear flow regime is recognized as a 1:2 slope (Dmour and Shokir 2010).

## 1.3 Reservoir Characterization

Throughout the last few years, the focus on reservoir characterization and pressure response analysis methods has increased tremendously. The reasons behind such interest are the difficulties faced throughout all attempts administrated to acquire reservoir parameters. Such difficulties create a lack in information needed to understand the complex nature of the unconventional resources. Therefore, different approaches and tools are invented and created in order to understand those resources.

### 1.3.1 Analytic Approaches

Different techniques and methods are used to conduct fracture analysis and reservoir performance characterization. These techniques have been examined and analyzed in many studies (Wattenbarger et al. 1998; Aanonsen et al. 2009; Khan and Callard 2010). However, their applications are constrained by few limitations and restrictions.

Wattenbarger et al. (1998) framed a method where reservoir behavior is examined at the linear flow stage for stimulated reservoirs with infinite conductivity fractures. The method uses a reservoir with a rectangular drainage area and a fracture that extends to the boundaries. The length extending from the boundaries of the reservoir and is perpendicular to the fracture is defined by the term ($y_e$) as shown in **Fig. 6.** The conductivity of the

fracture is assumed to be infinite ($C_{fD} > 50$) where $C_{fD}$ is defined by Eq. 1 mentioned above.

$$C_{fD} = \frac{k_f\, w}{k\, x_f}$$

Where the terms ($k_f$) and ($x_f$) are the hydraulic fracture permeability and half-length, respectively. The parameter (w) is the fracture width and (k) is the permeability.

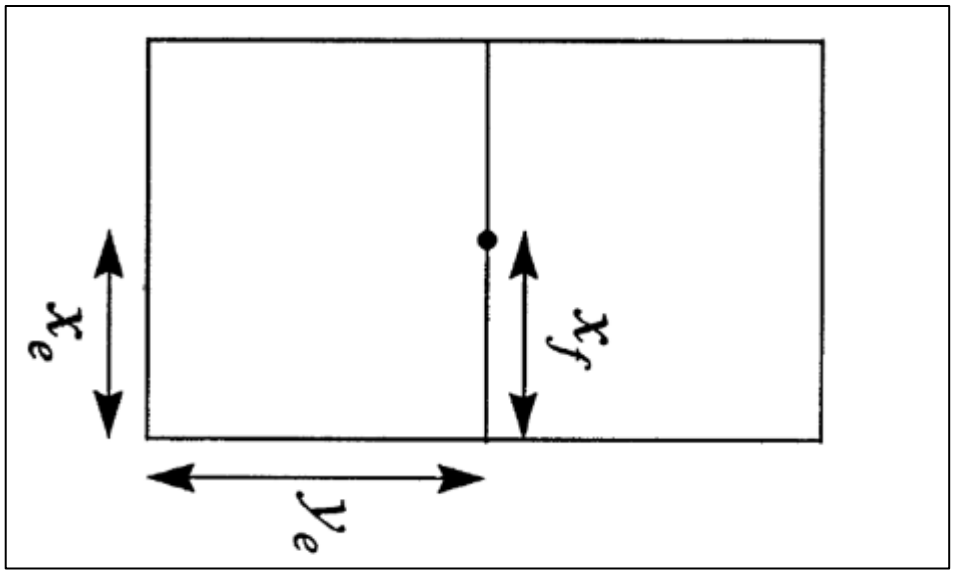


**Figure 6 - Top view of a rectangular reservoir with a fracture extending to the boundaries (after Wattenbarger et al. 1998).**

The study was conducted to model infinite conductivity fractures and find solutions for linear flow of fractures forecasting. The following equations describe the solutions for inner boundaries set by constant rate and flowing bottomhole pressure ($P_{wf}$)in a closed linear reservoir, separately.

*Constant Rate Condition*

$$P_{wD} = \frac{\pi}{2}\left(\frac{y_e}{x_f}\right)\left[\frac{1}{3} + \left(\frac{x_f}{y_e}\right)^2 t_{Dx_f}\right] - \frac{2}{\pi^2}\left(\frac{y_e}{x_f}\right)\sum_{n=1}^{\infty}\left(\frac{1}{n^2}\right)\exp\left[-n^2\pi^2\left(\frac{x_f}{y_e}\right)^2 t_{Dx_f}\right] \quad (3)$$

*Constant Pressure Condition*

$$\frac{1}{q_D} = \frac{\frac{\pi}{4}\left(\frac{y_e}{x_f}\right)}{\sum_{n_{odd}}^{\infty} \exp\left[-\frac{n^2\pi^2}{4}\left(\frac{x_f}{y_e}\right)^2 t_{Dx_f}\right]} \tag{4}$$

The term ($y_e$) is the distance from fracture to outer boundary and (n) is the number of layers in a linear layered reservoir. The dimensional variables are defined by the following set of equations:

$$P_{wD} = \frac{kh(p_i - p_{wf})}{141.2qB\mu} \tag{5}$$

$$\frac{1}{q_D} = \frac{kh(p_i - p_{wf})}{141.2qB\mu} \tag{6}$$

$$t_{Dx_f} = \frac{0.00633kt}{\phi\mu c_t {x_f}^2} \tag{7}$$

The notations ($p_i$) and ($p_{wf}$) are the initial and bottomhole flowing pressure, respectively. The parameter (h) is the net thickness; (q) is oil flow rate; (B) is the oil formation volume factor; and ($\mu$) is the viscosity. The total compressibility is defined by ($c_t$) while the porosity and time are defined by ($\phi$) and (t), respectively.

Wattenbarger et al. (1998) used type curves to describe the solutions that were found. In order to give only one curve for all case for any rectangular geometry, the terms ($\left(\frac{x_f}{y_e}\right) P_{wD}$) and ($\left(\frac{x_f}{y_e}\right)\frac{1}{q_D}$) were plotted against ($t_{Dy_e}$) as shown in **Fig. 7**. This study was conducted for both liquid and gas wells.

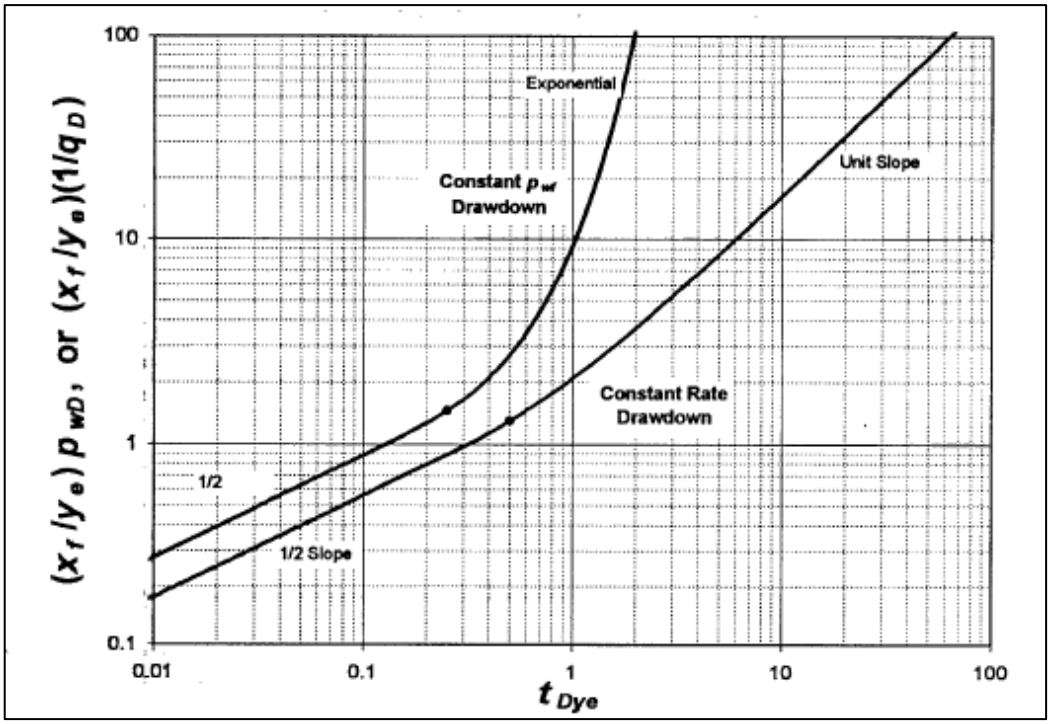


**Figure 7 - Solutions for constant rate and pressure conditions for a closed linear reservoir with infinite conductivity fractures (after Wattenbarger et al. 1998).**

Khan and Callard (2010) formulated a new technique and type curve that analyzes reservoir behavior during linear and bilinear flow regimes. This method utilizes the data provided in order to evaluate reservoir parameters in finitely conductive fractured reservoirs. The techniques assume a formation and fracture with characteristics and geometries like the ones used by (Wattenbarger et al. 1998) shown in **Fig. 8**.

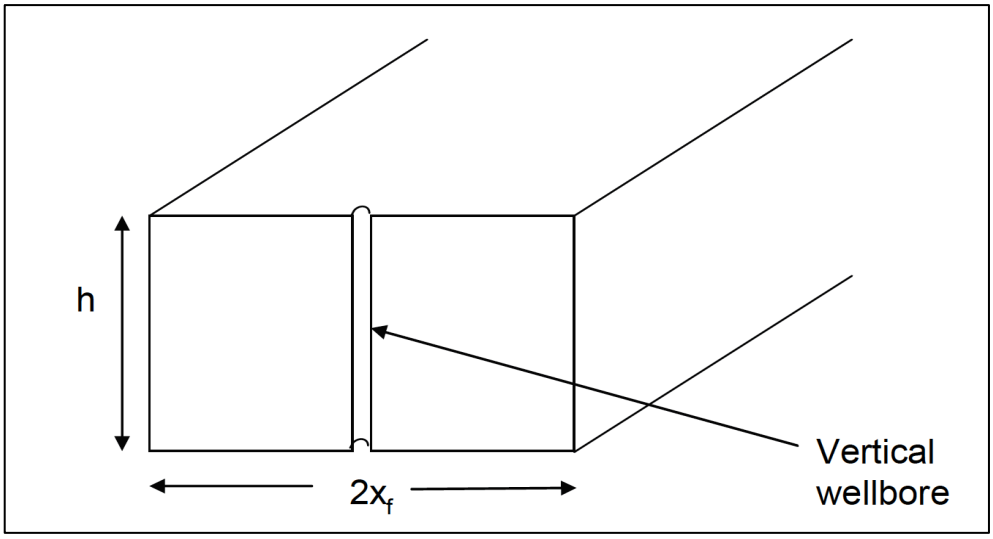


**Figure 8 - A rectangular reservoir with a thickness (h) (after Khan and Callard 2010).**

Khan and Callard (2010) formulated a new type curve to model the intersection of well flow and the finitely conductive fracture flow. The equations used to derive the type curves are defined for both bilinear and linear flows. The solution relating the dimensionless reciprocal rate and time in the bilinear flow (Bennett et al. 1986) as follows:

$$\frac{1}{q_D} = \frac{2.722}{\sqrt{C_{fD}}}\, {t_{Dx_f}}^{0.25} \tag{8}$$

Where the dimensionless variables are defined by:

$$\frac{1}{q_D} = \frac{kh\left(m(p_i) - m(p_{wf})\right)}{1422qT} \tag{9}$$

$$t_{Dx_f} = \frac{0.00633kt}{\phi\mu c_t {x_f}^2} \tag{10}$$

The term $(q_D)$ is the dimensionless flow rate and (T) is the reservoir temperature. The term $\left(m(p)\right)$ is the real gas pseudo pressure. The linear dimensionless reciprocal rate-time relation for the linear flow is defined as follows:

$$\frac{1}{q_D} = \frac{\pi^{1.5}}{2}\sqrt{t_{Dx_f}} \tag{11}$$

This equation can be written in its dimensional form:

$$\frac{1}{q} = m_{cp}\sqrt{t} \tag{12}$$

Where $(m_{cp})$ is the slope of $1/q_g$ and $\sqrt{t}$ and is defined as:

$$m_{cp} = \frac{315.2T}{h\sqrt{\phi(\mu c_t)_{P_{fP}}}}\frac{1}{[m(p_i)-m(p_{wf})]\sqrt{kx_f}} \tag{13}$$

The subscript $(P_{fP})$ defines the pressure at which properties are formulated. The intercept in a plot of the dimensionless reciprocal rate against square root time is greater than zero. Therefore, the equation describing that relationship is defined by:

$$\frac{1}{q_D} = \frac{\pi^{1.5}}{2}\sqrt{t_{Dx_f}} + \frac{1}{q_{D_i}} \tag{14}$$

The relationship is also exhibited by a numerical simulation of a provided model show the relationship as:

$$\frac{1}{q_D} = \frac{1}{\hat{q}_{D_i}} + \frac{\pi^3}{8}Q_D \tag{15}$$

The term $(Q_D)$ is the dimensionless cumulative production. Eq. 15 can also be written in the following dimensional form:

$$\frac{1}{q} = \frac{1}{\hat{q}_i} + \frac{{m_{cp}}^2}{2}G_P \tag{16}$$

The notation $(G_P)$ is the cumulative gas production. Comparing the dimensional form of the previous equation and the rate-cumulative hyperbolic form of Arps equation with 2 for the b exponent (Arps 1956) defined by:

$$\frac{1}{q} = \frac{1}{\hat{q}_i} + \frac{D_i}{{\hat{q}_i}^2}G_P \tag{17}$$

An identity can be formulated to relate the intimal decline rate ($D_i$) and the term ($m_{cp}$). This helps in utilizing Arps equation in describing the linear flow period of the reservoir. This identity is shown below.

$$D_i = \frac{\hat{q}_i{}^2 m_{cp}{}^2}{2} \tag{18}$$

The term ($D_i$) is the initial decline rate. The cumulative production rate-time relation described by Arps equation with b exponent of 2 (Arps 1956) is:

$$\frac{D_i}{2\hat{q}_i{}^2} G_P{}^2 + \frac{1}{\hat{q}_i} G_P - t = 0 \tag{19}$$

The bilinear and linear flows can be noticed in a type curve plot of reciprocal rate against time both multiplied by dimensionless fracture conductivity as seen in **Fig. 9.**

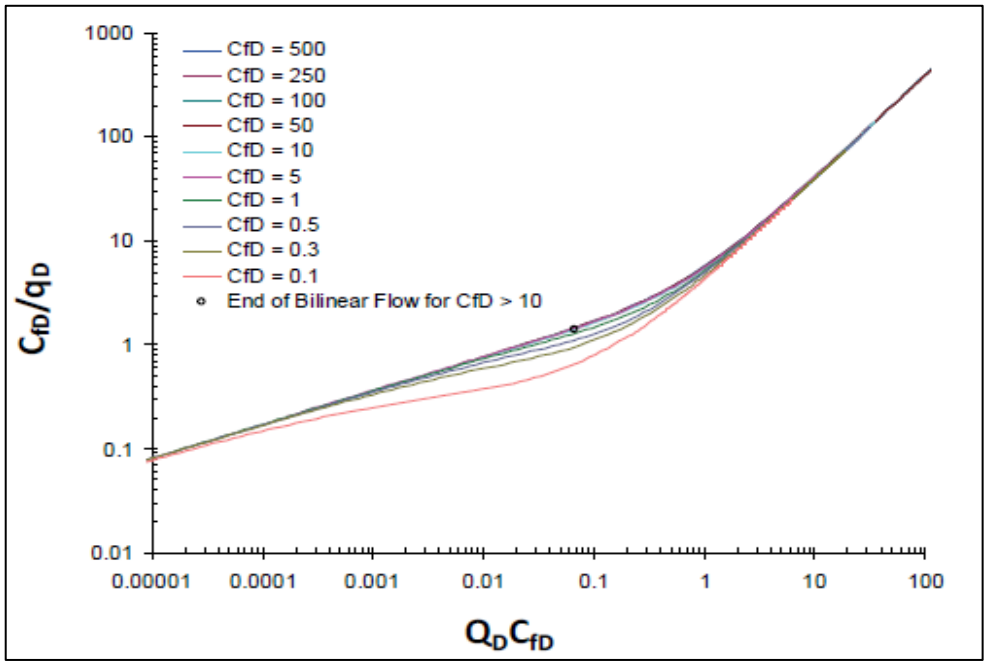


**Figure 9 - Type curve showing the Bilinear and Linear flow of a reservoir model (after Khan and Callard 2010).**

Rodrigues and Callard (2012) perform production analysis on a horizontal well with constant pressure production. The schematics of **Fig. 10**

are used to identify the linear flow period as well as the boundary dominated flow.

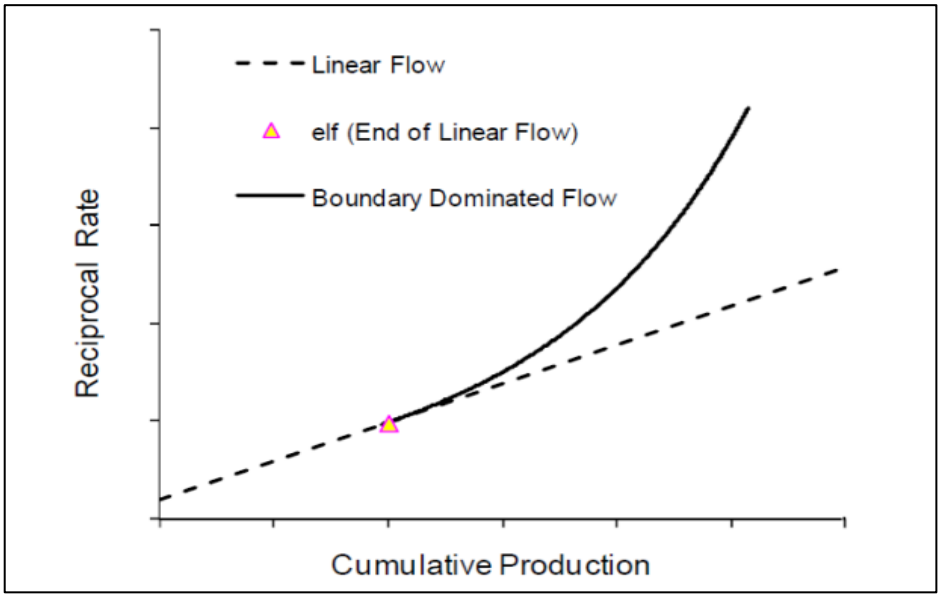


**Figure 10 - Flow Periods of constant pressure production in a gas well (after Rodrigues and Callard 2012).**

The flow regimes of Fig. 10 are described by Arps hyperbolic equation with b exponent of 2 (Arps 1956) as follows:

$$\frac{1}{q} = \frac{1}{q_i} + m_{rrc}Q \tag{20}$$

The term $(\frac{1}{\hat{q}_i})$ is the intercept, $(m_{rrc})$ is the slope, and (Q) is the cumulative production. The relationship between the initial decline rate and the intercept and slope is described by

$$D_i = {q_i}^2 m_{rrc} \tag{21}$$

The end points of the linear flow regimes are used to identify the rates at the boundary flow, which are equal to ending rates of the linear flow regimes described by $(q_{elf})$. Utilizing the cumulative production at the linear flow end point $(Q_{elf})$, the following can be generated:

$$\frac{1}{q_{elf}} = \frac{1}{q_i} + m_{rrc} Q_{elf} \quad (22)$$

The initial decline of rate of the boundary flow regime ($D_{ielf}$) is equal to the ending decline of the linear flow regime. This decline can be described using Arps equation

$$D_{ielf} = \frac{D_i}{(1+2D_i t_{elf})} \quad (23)$$

Utilizing the set of equations mentioned earlier, few reservoir and fracture parameters can be inferred. The permeability can be estimated using the following equation:

$$k = 31.0 \frac{\phi(\mu c_t)_{P_{fP}} {y_e}^2}{t_{elf_{CP}}} \quad (24)$$

where

$$t_{elf_{CP}} = \frac{m_{rrc}}{2} {Q_{elf}}^2 + \frac{1}{q_i} Q_{elf} \quad (25)$$

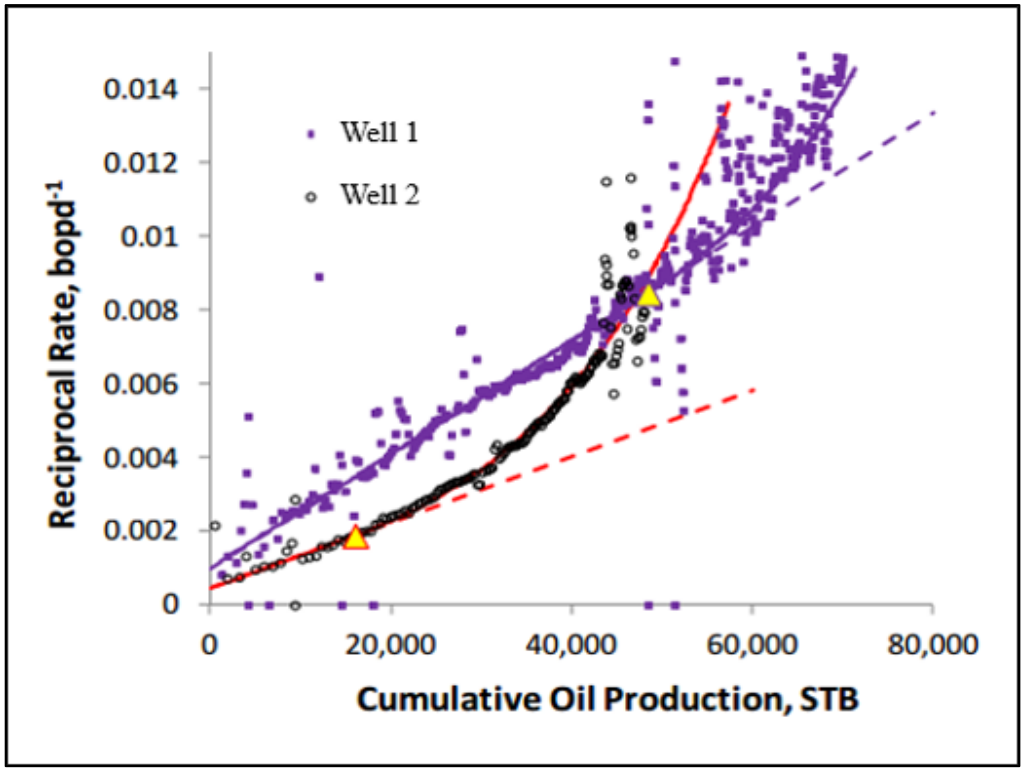


**Figure 11 - An example of Reciprocal Rate against Cumulative Production plot (Modified after Rodrigues and Callard 2012).**

The figure above, **Fig. 11** shows an example of the reciprocal rate plotted against cumulative production. The plot shows two wells; each with different end points of the linear flow. The slope of this plot can be used to calculate the half-length of the fracture using the equation below:

$$\sqrt{k}x_f = \frac{315.4T}{h\sqrt{2m_{rrc}\phi}} \tag{26}$$

The half-length of the fracture can be estimated by dividing the equation above by the permeability found through utilizing the equation generated earlier.

Although the formulations can be used adequately to estimate reservoir and fracture parameters, they have few limitations. The shortcomings of these methods lay in the assumptions made in formulating the techniques.

Homogeneity, uniformity, and linearity are few of many assumptions made. In addition, they require long running time and complicated calculations.

### 1.3.2 Semi-analytic and Numerical Approaches

In addition to analytic techniques to interpret pressure-rate data for formation/fracture properties, there are other techniques that are based on an inverse modeling approach. These techniques are classified as pure deterministic (analytic), full probabilistic (Stochastic, geostatistical, and statistical), or heuristic.

One of the more popular models for history matching/data assimilation is the Ensemble Kalman Filter (Evensen 2003; Gu and Oliver 2007; Aanonsen et al. 2009; Arroyo-Negrete et al. 2008). It is a sequential Monte Carlo technique that allows for continuous updates of a suite or ensemble of reservoir model. The relationship between the measurements and the model parameters are expressed using a covariance matrix and the assumption behind the method is that the model is linear and all model parameters are normally distributed. The basic equation for a linear system are shown in the following set of equations:

$$y_n^f = A y_{n-1}^a \tag{27}$$

$$y_n^a = y_n^f + K_n\left(d_{obs,n} - H y_n^f\right) \tag{28}$$

$$K_n = C_{y_n^f} H^T \left(H\, C_{y_n^f} H^T + C_{d_n}\right)^{-1} \tag{29}$$

$$C_{y_n^f} = A C_{y_{n-1}^a} A^T + C_\varepsilon \tag{30}$$

$$C_{y_n^a} = (1 - K_n H) C_{y_n^f} \tag{31}$$

The coefficient (y) is the estimated state vector for the system while the term ($d_{obs}$) are the measurements. The matrices ($C_\varepsilon$), ($C_y$) and ($C_d$) are the covariance matrices for the model noise, state vector of the system, and the measurements error, respectively. The subscripts (f), (a), and (n) represent the forward step, analysis step, and time index, respectively. The matrix (A) defines the dynamics of the system and Matrix (H) defines the linear relationship between the measurements and the states; while (K) is the Kalman gain matrix. Despite its popularity, this method contains few limitations. The main issue encountered is the constant updating of the covariance matrix in high-dimensional systems. Additionally when the ensemble size is kept small for computational efficiency, there may be a loss of variability and ensemble collapse (Arroyo-Negrete et al. 2008). Additional limitations arise because of non-Gaussian state variables, nonlinearity in system equations and non-Gaussian model errors.

### 1.4 Problem Statement

Well test analysis utilizes the pressure response to production or injection to infer formation and hydraulic fracture-related properties. Given a reservoir model, it is possible to extract information about the dimensionless fracture conductivity, fracture half-length and formation permeability from

well test data. However, as with decline curve analysis, long-term production or well test data is required for these low permeability shales.

Additionally, the approaches in Khan and Callard (2010) and Wattenbarger et al. (1998) share the same limitations such as:

1. The reservoirs are rectangular with a uniform thickness.
2. The formation is isotropic and homogenous.
3. The fracture and formation flow is uniform and linear.
4. The fractures are horizontal and their extent outlines the width of the reservoir.

These assumptions restrict the class of models that may be analyzed for formation- and completion-related properties. The method proposed in this thesis is based on earlier work by Vasco and Karasaki (2006) that utilizes the low frequency content of the bottomhole pressure data to infer hydraulic fracture permeability or conductivity. The advantage of the proposed approach is that it relies on the use of numerical simulation tools and therefore can easily be generalized to complex reservoirs and complex fracture networks and well architecture. Additionally, because only the low frequency content of the pressure data is utilized to infer formation/fracture properties, the method is robust in the presence of noise, which is typically characterized by high frequency variations. Moreover, by working in the frequency domain, the number of observations required in the inversion procedure is dramatically reduced.

The calculations and derivation of the asymptotic inversion approach are discussed later in the paper. Appendix C provides a full explanation of the governing equations used for pressure inversion and sensitivity analysis.

# Chapter 2: Mathematical Formulation

The central idea behind the approach adopted in this thesis is to utilize the frequency content of bottomhole pressure data to estimate reservoir/completion properties such as formation permeability and fracture conductivity. This allows for interpretation of fracture characteristics irrespective of the geometry of the fracture and can easily be generalized to heterogeneous media. The key drawback of analytic approaches is that they are limited to a small subset of possible well/fracture geometries and typically rely on assumptions of homogeneity and uniform formation thickness.

The steps in deriving the pressure inversion solution are listed in the next few sections. The formulation starts transformation of the diffusivity equation to the frequency domain. The reasons behind this domain transformation is discussed in details in later sections. In the frequency domain, the pressure equation is truncated to only consider low frequency variations in the pressure signal. Finally, the sensitivity of the pressure amplitudes to changes in gridblock permeabilities are computed. The derivation of the sensitivity equation is thoroughly discussed in Chapter 3.

In order to transform the pressure equation from the time domain to the low frequency domain, the application of the Fourier Transform and the vector differential operators are needed. A basic explanation of both concepts is provided in this chapter. Moreover, Gradshteyn and Ryzhik (1980) provide detailed explanation of the Fourier Transform. In addition, Appendix C

provides all the steps taken to generate the final forms of the equations of the derivation.

## 2.1 Methodology

Evaluation of pressure responses post-hydraulic fracturing is essential to quantify fracture geometries and formation permeabilities. Vasco and Karasaki (2006) have investigated an asymptotic solution of low frequency transient pressure variations to estimate formation permeability for cross-well tests. The use of this approach is conducted through applying constant rate tests that are run for specific periods of time. The pressure is monitored at one or several locations at the injection/producing well and these are interpreted to provide an estimate of interwell connectivity. In this work, I adopt this low-frequency asymptotic approach to estimate fracture conductivities.

Pressure data, especially bottomhole pressure data, often comprises of large datasets that are accompanied by noise. The low frequency asymptotic approach utilizes the frequency domain to reduce the amount of data needed to determine formation properties. This is done by truncating the pressure equation in the frequency domain to only account for low frequency components of the pressure. The formulation of transforming the pressure equation to the low frequency domain is explained in section 2.4.

This study focuses on using the low frequency approximation of the diffusivity equation, the pressure equation, because of the following assumptions:

1. The high frequency variations are sensitive to noise in the measurements.
2. The low frequency responses correspond to lateral and vertical variations in the reservoir/completion properties.
3. Working in the frequency domain reduces the number of bottomhole pressure observations needed for fracture properties estimation, significantly.
4. The method can easily be generalized to many different reservoir and testing scenarios.
5. The final form of the semi-analytical approach is independent of the number of frequencies chosen and can therefore be easily solved.
6. The high frequency approximations require computations that can be difficult to achieve due to background and well effects.

## 2.2 Fourier Transform

The Fourier transform is a method typically used to break down the waveform to its simplest representations. This function transforms between signals in the time and frequency domains. It is usually associated with periodicity and repetition descriptors such as frequency (periodicity of time) and periods (periodicity in space). Fourier Transform is defined by the following integrals (Gradshteyn and Ryzhik 1980):

Synthesis (Inverse Solution) $f(t) = \frac{1}{2\pi} \int_{-\infty}^{+\infty} F(\omega) e^{i\omega t}\, d\omega$ (32)

Analysis (Forward Solution) $$F(\omega) = \int_{-\infty}^{+\infty} f(t)e^{-i\omega t}\, dt \quad (33)$$

Where *F* is the Fourier transform of function *f*, while $\omega$ and t are angular frequency and time, respectively. The notations describing the Fourier Transform Integral were specifically chosen to suit the parameters and notations used later in the mathematical formulation of the study. The transform utilizes the periodical characteristics of the sine and cosine through the use of Euler's Formula:

$$e^{i\emptyset} = \cos\emptyset + i\ \sin\emptyset \quad (34)$$

## 2.3 Derivation of the Pressure Equation

In order to derive a mathematical expression that effectively describes the pressure variations with time and space in multiphase medium, few basic governing equations must be used (Peaceman, 1977). These equations are Mass Balance equation, Darcy's Law, and the Equation of State. Integrating and solving the three equations will generate the diffusivity equation described in Eq. 35 below.

$$\mathrm{c}(\nabla p)^2 + \nabla^2 p = \frac{\phi \mu c_t}{k}\frac{\partial p}{\partial t} \quad (35)$$

The coefficients (c) and ($c_t$) are the fluid and total compressibilities, respectively. The term (p) is the pressure and (k) is the permeability. The porosity is defined by ($\phi$) and the viscosity is defined by (μ).

Starting our derivation by incorporating multiphase flow parameters in Darcy's Law illustrated in Eqs. 36. In this case, two flowing phases are applied

and are defined by the subscripts (n) and (w) denoting the nonwetting and wetting phases, respectively. It must be noted that the two flowing phases, wetting and nonwetting, flow concurrently and hence interfere with each other's flow. Therefore, the concept of relative permeability is utilized and Darcy's law equations are rewritten in the multiphase form as follows:

$$\vec{v}_n = -\frac{Kk_{rn}}{\mu_n}\left(\nabla p_n + \rho_n g \nabla \mathrm{D}\right) \tag{36a}$$

$$\vec{v}_w = -\frac{Kk_{rw}}{\mu_w}\left(\nabla p_w + \rho_w g \nabla \mathrm{D}\right) \tag{36b}$$

Here ($v$) is the superficial velocity and (K) is the absolute permeability. The terms ($k_r$) and ($\mu$) define the relative permeability and viscosity, respectively. In addition, ($g$) is the gravitational acceleration; ($\rho$) is the density; and ($D$) is the parameters depth. The single phase form of the Material Balance equation can be utilized to incorporate the two flowing phases, as in Eqs. 37.

$$\nabla \cdot (\alpha \rho_n \vec{v}_n) + \alpha q_n = -\alpha \frac{\partial(\phi \rho_n S_n)}{\partial t} \tag{37a}$$

$$\nabla \cdot (\alpha \rho_w \vec{v}_w) + \alpha q_w = -\alpha \frac{\partial(\phi \rho_w S_w)}{\partial t} \tag{37b}$$

The notations ($S$) and ($\phi$) denote the saturation and porosity values of the wetting and nonwetting phase. The term ($\alpha$) is a geometric factor function. This function is added in order to be able to use the same equation for any number of dimensions (Peaceman, 1977). Expanding the time derivative terms of the continuity equations illustrated by Eqs. 37 produces:

$$\nabla \cdot (\alpha \rho_n \vec{v}_n) + \alpha q_n = -\alpha \left[\rho_n S_n \frac{\partial \phi}{\partial t} + \phi S_n \frac{d\rho_n}{dp_n}\frac{\partial p_n}{\partial t} + \phi \rho_n \frac{\partial S_n}{\partial t}\right] \tag{38a}$$

$$\nabla \cdot (\alpha \rho_w \vec{v}_w) + \alpha q_w = -\alpha \left[\rho_w S_w \frac{\partial \phi}{\partial t} + \phi S_w \frac{d\rho_w}{dp_w}\frac{\partial p_w}{\partial t} + \phi \rho_w \frac{\partial S_w}{\partial t}\right] \tag{38b}$$

Since these two phases are the only fluids flowing in the pores, the saturations are defined by ($S_n + S_w = 1$). The two sets of Eqs. 38 are divided by the terms $\alpha\rho_n$ and $\alpha\rho_w$, respectively. The average pressure and phase mobilities are given by:

Average Pressure: $$p_{avg} = \frac{p_n + p_w}{2} \quad (39)$$

Phase Mobilities - Nonwetting $$\lambda_n = \frac{Kk_{rn}}{\mu_n} \quad (40a)$$

Phase Mobilities – Wetting $$\lambda_w = \frac{Kk_{rw}}{\mu_w} \quad (40b)$$

In order to generate the final form of the equation needed for pressure variations, Darcy's law described by Eqs. 36 are substituted into the produced continuity equations of Eqs. 38a and 38b after division. Similarly, the constraint equation ($S_n + S_w = 1$), the average pressure shown in Eq. 39, and phase mobilities, defined by Eqs. 40a and 40b, are incorporated in the same resultant Eqs. 38. A fully detailed derivation of the pressure equation can be found in Appendix B. The following equation defines the final form of pressure variations $P(x,t)$:

$$\nabla(K\lambda_t) \cdot \nabla P + K\lambda_t \nabla \cdot \nabla P = C\frac{\partial p}{\partial t} \quad (41)$$

Where the term ($\lambda_t$) denotes the total mobility defined as:

$$\lambda_t = \frac{k_{rn}}{\mu_n} + \frac{k_{rw}}{\mu_w} \quad (42)$$

The Coefficient (C) is given by:

$$C = \frac{d\phi}{dP} + \phi c_n S_n + \phi c_w S_w \quad (43)$$

The terms ($c_n$) and ($c_n$) are the nonwetting and wetting phase compressibilities, respectively. Total mobility does not vary significantly with position (x) thus it will be treated as a constant. The dependency of coefficient (C) on time can be neglected when the compressibilities are similar and the medium is not deformed, as a result of the saturation constraint ($S_n + S_w = 1$) mentioned above. Therefore, coefficient (C) is assumed to independent of time but dependent on space.

The pressure variations $P(x, t)$, described in Eq. 41 above, is considered to be the basis of the asymptotic model derivations.

## 2.4 Low Frequency Asymptotic Solution

In this study, an asymptotic inversion technique is utilized to interpret and invert pressure variations in the low frequency domain. Working in the frequency domain requires the transformation of the pressure variations through the Fourier Transform discussed above. Transforming the pressure to the frequency domain reduces the volume of observation data to a much smaller quantity of observations.

The pressure data in the frequency domain is then utilized to characterize the reservoir and the completions. This is accomplished through the use of inverse methods and model parameter sensitivities. Sensitivities are defined as the change in the output to a change in the input. In this specific problem, the sensitivities refer to changes in the pressure data in the frequency domain to changes in gridblock permeability values. Sensitivities can be

computed either analytically or numerically. Numerical sensitivities can be computed by changing the value of each gridcell permeability, then running Eclipse to predict bottomhole pressure variations. The bottomhole pressure variations are estimated every time the permeability in each single gridblock is altered. This is repeated N+1 times, where N is the number of gridcells and the additional simulation run is for the reference model. The sensitivities to changes in gridcell permeabilities is then computed as change in bottomhole pressure to a corresponding change in gridcell permeabilities. Eventually this will result in sensitivity values for each gridcell for each well in the model. The main disadvantage of numerical sensitivity computations is the need for several simulation runs. This can become prohibitively expensive when considering large field-scale studies.

In this work, I overcome the problems associated with numerical sensitivity computation by analytically computing them. Analytical Sensitivity calculations are discussed later in the chapter.

The main purpose of the asymptotic approach is to find a solution for the diffusive pressure component that emulates the characteristics of the wave propagation model. Virieux et al. (1994) and many others have studied the asymptotic approach in deriving the diffusivity equation in the frequency domain. The following notation describes the general form of the solution to the diffusion equation in the frequency domain. The use of this equation is discussed later in the chapter.

$$\hat{P}(x,\omega) = \mathrm{w}(\mathrm{x},\omega)\,\frac{e^{-\sqrt{\omega}\,\sigma(x)}}{\sqrt{\omega}}$$

Virieux et al. (1994) explains that the diffusion equation when transformed depends on the expression $\exp(\sqrt{\omega})$. A similar factor $\exp(\omega^{1/3})$ appeared in the asymptotic solution of wave propagation model of Hilbert Transform. As a result of the observations found by Virieux et al. (1994), the diffusion equation in the frequency domain was defined in that specific form.

The asymptotic solution for the equation describing the diffusive component, pressure, is transformed to the frequency domain using a Fourier transform integral described in Eq. 44. Working in the low frequency or long period domain requires transforming P(x, t), pressure variations, a function of space(x) and time (t) to $\hat{P}(\mathrm{x},\omega)$. The term $\hat{P}(\mathrm{x},\omega)$ is defined as the pressure variations in the frequency domain as a function of space (x) and frequency ($\omega$).

$$\hat{P}(x,\omega) = \int_{-\infty}^{+\infty} e^{-i\omega t}\,P(x,t)\,dt \tag{44}$$

In order to describe the behavior of pressure variations in the frequency domain, the pressure is transformed through a Fast Fourier transform. As a result, the pressure (shown in Eq. 41) in the frequency domain becomes:

$$\nabla(K\lambda_t)\cdot\,\nabla\hat{P} + K\lambda_t\nabla\cdot\,\nabla\hat{P} = \omega C\hat{P} \tag{45}$$

Hydraulic permeability is presented by the term K(x) and the pressure variations in the frequency domain is defined by the term ($\hat{P}$). The term ($\omega$) is the frequency and the function (C) is defined by:

$$C = \frac{d\phi}{dP} + \phi c_n S_n + \phi c_w S_w$$

Pressure variations can also be described in the frequency domain through power series representations (Virieux et al. 1994):

$$\hat{P}(x,\omega) = \frac{e^{-\sqrt{\omega}\,\sigma(x)}}{\sqrt{\omega}} \sum_{n=0}^{\infty} P_n(x)\ \omega^n \tag{46}$$

The function $\sigma(x)$ is defined as the phase and (n = 0, 1, 2 …). This form of the pressure equation is adopted from the representation of the diffusivity equation in the frequency domain in a homogenous medium for an impulsive source (Virieux et al. 1994). This type of equation is dominated by the first few terms for when the magnitude of the frequency ($\omega$) is small. The solution of the pressure equation in uniform mediums is described by some form of a modified Bessel function of the zeroth order $K_0(\sqrt{\omega}\alpha r)$. The term $\alpha$ is a constant depending on medium properties and r is the distance from the source. The solution of the pressure variations, illustrated in Eq. 46, is an adaptation of the modified Bessel function for small frequency ($\omega$) (Vasco and Karasaki, 2006). The solution to the variation and the diffusion equation in the frequency domain is

$$\hat{P}(x,\omega) = \mathrm{w}(\mathrm{x},\omega)\frac{e^{-\sqrt{\omega}\,\sigma(x)}}{\sqrt{\omega}} \tag{47}$$

The expression $\mathrm{w}(\mathrm{x},\omega)$ depends on the orders of the frequency magnitudes and is defined by its series form as

$$\mathrm{w}(\mathrm{x},\omega) = \sum_{n=0}^{\infty} P_n(x)\,\omega^n \tag{48}$$

The pressure variation term in Eq. 48, defined by the expression $P_n(x)$, is a function of space (x). Note that in order to work in the low frequency domain, only the smallest magnitudes of frequency where ($\omega \ll 1$) were used.

Therefore, the representation of the pressure $\hat{P}(x,\omega)$ in Eq. 46 is significantly controlled by the first few terms. Accordingly, the final form of Eq. 46 can be used to adequately represent the pressure variations in the low frequency domain. This is shown in Eq. 49, where the term $P_0(\mathrm{x})$ is defined as the zeroth-order amplitude of the pressure variations.

$$\hat{P}(x,\omega) = \frac{e^{-\sqrt{\omega}\,\sigma(x)}}{\sqrt{\omega}}\, P_0(x) \tag{49}$$

In order to utilize the equation above to calculate the low frequency pressure variations for a given model, the terms $P_0(x)$ and $\sigma(x)$ need to be calculated. Substituting and solving Eqs. 47 or 46 into Eq. 45 generates a new set of terms characterized by different orders of frequency $(\omega)$. The mathematical operations conducted are summarized below. The terms $(\nabla)$ and $(\nabla \cdot \nabla)$ are spatial derivatives that are defined as the gradient and the Laplacian expressions, respectively. For straightforwardness reasons, only the final solutions for solving Eqs. 47 and 45 are described below. A step-by- step detailed mathematical formulation of the solution can be found in Appendix C.

*Pressure Gradient* $\nabla\hat{P}(x,\omega)$

$$\nabla\hat{P}(x,\omega) = \frac{e^{-\sqrt{\omega}\,\sigma(x)}}{\sqrt{\omega}} \left(\nabla \mathrm{w}(\mathrm{x},\omega) - \sqrt{\omega}\,\nabla\sigma(x)\,\mathrm{w}(\mathrm{x},\omega)\right) \tag{50}$$

*Pressure Laplacian* $\nabla\ \cdot \nabla\hat{P}(x,\omega)$

$$\nabla\ \cdot \nabla\hat{P}(x,\omega) = \frac{e^{-\sqrt{\omega}\,\sigma(x)}}{\sqrt{\omega}} \Big(\mathrm{w}(\mathrm{x},\omega)\omega\,\nabla\sigma(x)\,\nabla\sigma(x) - \sqrt{\omega}\,\nabla\cdot\nabla\sigma(x)\mathrm{w}(\mathrm{x},\omega) - 2\sqrt{\omega}\,\nabla\sigma(x)\big(\nabla \mathrm{w}(\mathrm{x},\omega)\big) + \nabla\cdot\nabla\, w(x,\omega)\Big) \tag{51}$$

Substituting the definitions of $\nabla\hat{P}(x,\omega)$ and $\nabla\cdot\nabla\hat{P}(x,\omega)$, described by Eqs. 50 and 51, into Eq. 45 generates the following equation:

$$K(x)\lambda_t\left(\mathrm{w}(\mathrm{x},\omega)\sqrt{\omega}\nabla\sigma(x)\,\nabla\sigma(x) - \nabla\cdot\nabla\sigma(x)\mathrm{w}(\mathrm{x},\omega) - 2\,\nabla\sigma(x)\nabla\mathrm{w}(\mathrm{x},\omega) + \omega^{-1/2}\nabla\cdot\nabla\, w(x,\omega)\right) + \nabla K(x)\lambda_t\left(\omega^{-1/2}\,\nabla\mathrm{w}(\mathrm{x},\omega) - \nabla\sigma(x)\,\mathrm{w}(\mathrm{x},\omega)\right) = \sqrt{\omega}\,C(x)\mathrm{w}(\mathrm{x},\omega) \quad (52)$$

The generated equation above represents the final form of Eq. 45 after substitution, factoring out the exponent term, and dividing both sides by the term $\sqrt{\omega}$. As mentioned earlier and as Eq. 48 indicates, the term $\mathrm{w}(\mathrm{x},\omega)$ depends on different orders of frequency. Therefore, the term $\mathrm{w}(\mathrm{x},\omega)$ was defined in power series form as seen in Eq. 48.

$$\mathrm{w}(\mathrm{x},\omega) = \sum_{n=0}^{\infty} P_n(x)\;\omega^n \quad (48)$$

If we were to substitute the power series form of Eq. 48 into Eq. 52, the solution will generate a sum of infinite number of expressions with varying orders of frequencies $\sqrt{\omega}$. Let us recall that we are aiming to working in the low frequency domain. Therefore, only frequencies ($\sqrt{\omega}$) of small magnitudes are considered.

The solution to deriving an equation of pressure variations in the low frequency domain is done through examining the terms of Eq. 52. The terms combined with the smallest orders of the term $\sqrt{\omega}$, are selected. The solutions to terms with $\sqrt{\omega}^{-1}$,$\sqrt{\omega}^{0}$, and$\sqrt{\omega}^{1}$ frequencies are discussed below.

**Terms of order$\sqrt{\omega}^{-1}$**

Examining terms with the smallest order $\sqrt[-1]{\omega}$ provides the equation defining the zeroth-order amplitude of the pressure variations $P_0(\mathrm{x})$.

$$K(x)\lambda_t \nabla \cdot \nabla P_0(\mathrm{x}) + \nabla [K(x)\lambda_t] \cdot \nabla P_0(\mathrm{x}) = 0 \quad (53)$$

The expression above is a first order differential equation that resembles the equation governing the steady state pressure. Note that the solution of the zeroth-order amplitude $P_0(\mathrm{x})$ equation depends on the total mobility $\lambda_t$ and the hydraulic permeability $K(x)$ . In addition, the solution of Eq. 53 is independent of frequency, thus, only one solution per well point is needed.

***Terms of order $\sqrt{\omega}^{0}$***

Examining terms with the second smallest order of frequency $\sqrt[0]{\omega}$, provides an equation needed to solve for the phase coefficient$\sigma(x)$.

$$\mathrm{K(x)}\lambda_t \, P_0(\mathrm{x}) \nabla \cdot \nabla \, \sigma(x) + \nabla [K(x)\lambda_t] \cdot P_0(\mathrm{x}) \, \nabla \sigma(x) + 2 \, \mathrm{K(x)}\lambda_t \nabla P_0(\mathrm{x}) \cdot \nabla \, \sigma(x) = 0$$

This equation shows the dependency characteristics of the phase coefficient on the zeroth-order amplitude $P_0(\mathrm{x})$, the total mobility $\lambda_t$, and the hydraulic permeability $K(x)$. In order to solve for the phase parameter, Eq. 53 must be solved first. The equation above can be rewritten in a more compact form using the coefficients and vector of coefficients defined below.

$$\Omega(x) \nabla \cdot \nabla \, \sigma(x) + \boldsymbol{\Upsilon}(\mathrm{x}) \cdot \nabla \sigma(\mathrm{x}) = 0 \quad (54)$$

Where the terms $\Omega(x)$ and $\boldsymbol{\Upsilon}(\mathrm{x})$ denote the scalar and vector coefficients mentioned above, respectively.

$$\Omega(x) = \mathrm{K(x)}\lambda_t \, P_0(\mathrm{x})$$

$$\boldsymbol{\Upsilon}(\mathrm{x}) = \nabla [K(x)\lambda_t] P_0(\mathrm{x}) + 2 \, \mathrm{K(x)}\lambda_t \nabla P_0(\mathrm{x})$$

The equations required to solve both the zeroth-order amplitude $P_0$(x) and phase coefficient σ(x) are both independent of the frequency. As a result only one solution per well is needed for each parameter.

***Terms of order*** $\sqrt{\omega}^{\mathbf{1}}$

Examining terms with the largest order of frequency $\sqrt[1]{\omega}$, provides an equation relating the zeroth-order amplitude $P_0$(x), the phase coefficient σ$(x)$, and the amplitude term $P_1(x)$.

$$\nabla \cdot [K(x)\lambda_t \cdot \nabla P_1] = [C(x) - \mathrm{K(x)}\lambda_t \nabla\sigma \cdot \nabla\sigma]P_0 \quad (55)$$

Solving for amplitude term $P_1(x)$ requires solutions for both Eqs. 53 and 54. Solution of the diffusive travel time in high frequency domain is described by the eikonal equation represented by the right side of Eq. 55.

In order to estimate the pressure variations in the frequency domain, both the zeroth-order amplitude pressure and the phase coefficients must be calculated using Eqs. 53 and 54. The equations governing $P_0(x)$ and $\sigma(x)$ are independent of the frequencies, therefore only one solution per well needs to be calculated.

# Chapter 3: Model Parameter Sensitivity Calculations

In this chapter, I discuss the analytic sensitivity calculations for variations in pressure amplitudes to changes in gridblock permeability values. In the previous chapter, I derived the frequency-domain form of the diffusivity equation and then derived the low-frequency approximation to describe pressure variations as a function of location and frequency.

The main purpose of the sensitivity calculations is to relate variations of a specific model parameter at **point y** to observations recorded at **point x**. In this study, the perturbation method is used to calculate model parameter sensitivities, which are essential parts of every iterative inverse method. In this study, the perturbations in hydraulic permeability $\delta k_j$ or $\delta k(y)$ located at **point y** are related to the observed values of the pressure change $\delta \hat{P}(x, \omega)$ in the well located at **point x**.

In order to assess the validity of the semi-analytic sensitivity computation, I also compare them to the numerical sensitivities for a synthetic case study that I will describe later in this section.

## 3.1 Semi-Analytical Sensitivity Calculations

The sensitivities are calculated through the comparison of hydraulic permeabilities at **point y** altered slightly from base or background permeability with value $K^b(y)$. The same method is used to compare changes created at the pressure at **point x** to a background or base model that has a

pressure of $\hat{P}^b(x,\omega)$. The comparisons made between the permeabilities and pressure before and after perturbations are shown in Eqs. 56 and 57:

$$\delta K(y) = K^b(y) - K(y) \tag{56}$$

$$\delta \hat{P}(x,\omega) = \hat{P}^b(x,\omega) - \hat{P}(x,\omega) \tag{57}$$

According to Vasco et al. (2000), an equation defining the term $\delta \hat{P}(x,\omega)$ can be derived. This is done through substituting the terms $k(y)$ and $\hat{P}(x,\omega)$ into Eq. 45 and focusing on the first order terms in the perturbation. If we were to solve Eq. 45 after substitution, the equation would be identical to static pressure equation with additional source terms.

Using Green's function solution $\nabla G(x,y,\omega)$, the term $\delta \hat{P}^b(x,\omega)$ can be calculated through integrating over a volume, **V**. The resultant formula is shown below:

$$\delta \hat{P}(x,\omega) = -2 \int_V \nabla G(x,y,\omega) \cdot \nabla \hat{P}^b(y,\omega) \delta k(y) dy \tag{58}$$

The term $\nabla G(x,y,\omega)$ describes the pressure variations at **point x** due to perturbations at source **point y**. Applying the asymptotic technique and making use of Eq. 49, Green's function in frequency domain becomes:

$$G(x,y,\omega) = P_0(y,x) e^{-\sqrt{\omega}\sigma(y,x)} \psi(\omega) \tag{59}$$

The term $\psi(\omega)$ represents the coefficients that are dependent on frequency. Pressure $P_0(y,x)$ is described as the pressure amplitude at **point x** due to perturbations at source **point y**. A similar zeroth order representation is generated for $P^b(x_s,y,\omega)$ where pressure amplitude variations at **point y** due to a source at **point $x_s$**:

$$P^b(x_s, y, \omega) = P_0(x_s, y)e^{-\sqrt{\omega}\sigma(x_s,y)}\psi(\omega) \quad (60)$$

The expression $\sigma(y, x)$ describes the phase at **point x** due to perturbations at source **point *y*** and $\sigma(x_s, y)$ describes the phase at point **y** due to a source at **point $x_s$**. The spatial gradients of terms $G(x, y, \omega)$ and $P^b(x_s, y, \omega)$ are expressed as:

$$\nabla G(x, y, \omega) = \nabla P_0(y, x)e^{-\sqrt{\omega}\sigma(y,x)}\psi(\omega)$$
$$-\sqrt{\omega}\nabla\sigma(y, x)P_0(y, x)e^{-\sqrt{\omega}\sigma(y,x)}\psi(\omega) \quad (61)$$

$$\nabla P^b(x_s, y, \omega) = \nabla P_0(x_s, y)e^{-\sqrt{\omega}\sigma(x_s,y)}\psi(\omega)$$
$$-\sqrt{\omega}\nabla\sigma(x_s, y)P_0(x_s, y)e^{-\sqrt{\omega}\sigma(x_s,y)}\psi(\omega) \quad (62)$$

Substituting and solving Eqs. 61 and 62 into the expression defined by Eq. 58, the following is generated:

$$\delta\hat{P}(x, \omega) = -2\int_V \nabla P_0(y, x) \cdot \nabla P_0(x_s, y)\psi^2(\omega)$$
$$\times e^{-\sqrt{\omega}[\sigma(x_s,y)+\sigma(y,x)]}\,\delta K(y)dy \quad (63)$$

Using only low frequency values by disregarding higher frequencies and assuming the expressions defined by Eqs. 64 and 65, we can define Eq. 63 in a more compact form as shown in Eq. 66.

$$\sum(x_s, x) = \sigma(x_s, y) + \sigma(y, x) \quad (64)$$

$$\Pi(x_s, x, \omega) = -2\,\nabla P_0(y, x) \cdot \nabla P_0(x_s, y)\psi^2(\omega) \quad (65)$$

As mentioned above, the following equation is achieved through substitutions of Eqs. 64 and 65 into Eq. 63:

$$\delta\hat{P}(x, \omega) = \int_V \Pi(x_s, x, \omega)e^{-\sqrt{\omega}\,\Sigma(x_s,x)}\,\delta k(y)dy \quad (66)$$

The final term describing the resultant variations of observed pressure at **point x** due to hydraulic permeability perturbations at **point y** is:

$$\frac{\delta \hat{P}(x,\omega)}{\delta k(y)} = \Pi(x_s, x, \omega) e^{-\sqrt{\omega}\,\Sigma(x_s,x)} \tag{67}$$

It must be noted that if the source **points $\mathbf{x_s}$** and **x** are not situated in the same location, a total of four solutions needed. Two solutions of phase and zeroth-order amplitude per point is needed to be able to solve for sensitivities. However, if the source **points $\mathbf{x_s}$** and **x** are in the same location, only two solutions are needed to calculate and measure model parameters sensitivities.

In the case of this study, both source **points $\mathbf{x_s}$** and **x** are in the same location. Therefore, the sensitivities for this single source well is defined by the square of the pressure gradient as shown in Eq. 68. The phase coefficient needs not to be calculated at frequencies ($\omega = 0$) as it is automatically dropped.

$$\frac{\delta \hat{P}(x,\omega)}{\delta k(y)} = -2\,\nabla P_0(x,y) \cdot \nabla P_0(x,y) e^{-\sqrt{\omega}\sigma(y,x)} \tag{68}$$

### 3.2 Numerical Sensitivity Calculations

The main reason behind calculating sensitivities is to assess the validity of the semi-analytical approach that was discussed above. In addition, both the semi-analytic and the numerical sensitivities were applied to a base model for comparison purposes. This base model consists of a 21x21x1 cell reservoir with a producing well in the middle of mesh as shown in **Fig. 12**. The uniform permeability of the reservoir formation is 8.12 millidarcies and the uniform porosity is 10%. The initial water saturation of the reservoir is 22.1%. The

initial pressure of the reservoir is 3000 psi and the well is set to produce at a rate of 35 bbl/D.

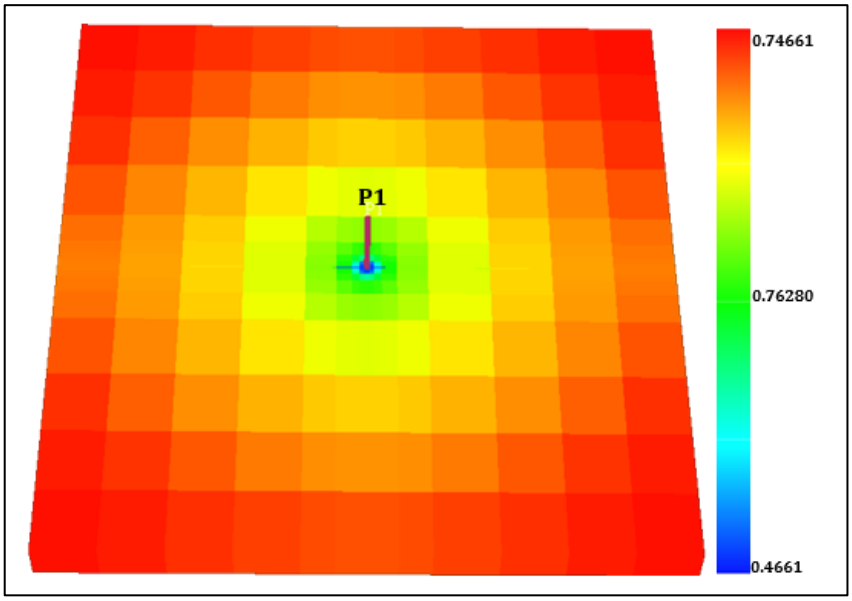


**Figure 12 - A synthetic model with a producing well placed at cellblock 11x11x1.**

The first step to computing the numerical sensitivities was perturbing the permeabilities of each of the gridblocks one at a time. This is done by perturbing the permeability of a gridblock by 5% and re-computing the bottomhole pressure at the observation well by running Schlumberger Eclipse. The unperturbed and the perturbed pressure variations are Fourier transformed into the frequency domain. The difference between the two frequency-domain pressures is then calculated and divided by the permeability differences for the chosen gridblock to obtain the numerical sensitivity for that gridblock. The model used in this work has a 21x21x1 mesh and therefore, the total number of simulation runs is 442.

The resultant numerical sensitivities for the base model are shown in **Figs. 13 and 14.** The numerical sensitivities calculated for the base model were

calculated for two different frequencies. The sensitivities for the two frequencies agree in their patterns. The most sensitive areas are concentrated around the well.

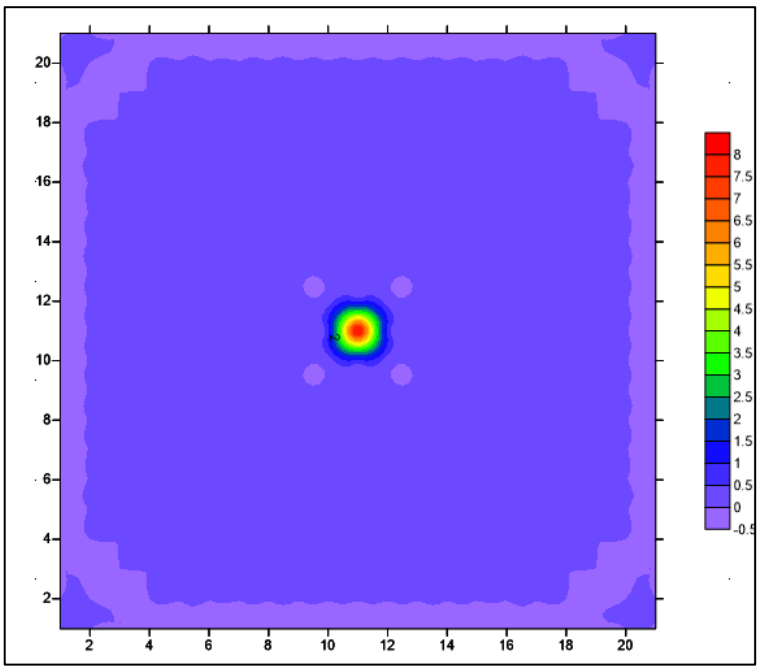


**Figure 13 - Numerical Sensitivity Model for Frequency 1.**

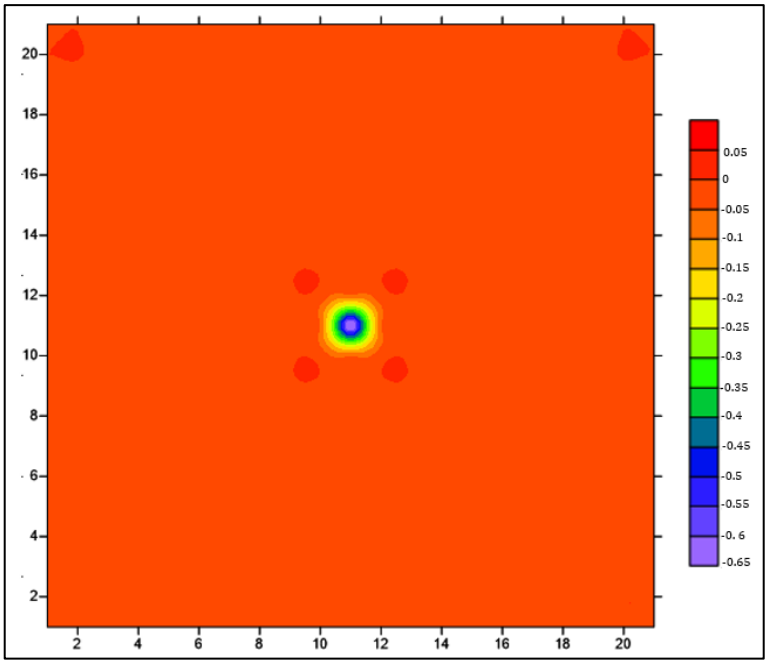


**Figure 14 - Numerical Sensitivity Model for Frequency 2.**

The semi-analytical sensitivities calculated for the same base model are shown in **Fig. 15.** The semi-analytical sensitivities were calculated only for Frequency 1. Examining Fig. 13 and comparing to Fig. 15, we see excellent correspondence in terms of the sensitivity patterns. The advantage of the semi-analytic sensitivity computation is that is requires only two full field simulation runs and therefore provides for two orders of magnitude reduction in the number of simulation runs required. The sensitivities shown in Figs. 13 and 14 provide validation for the semi-analytic sensitivities derived earlier. I can now use this in an inverse scheme to estimate gridblock permeabilities using pressure data.

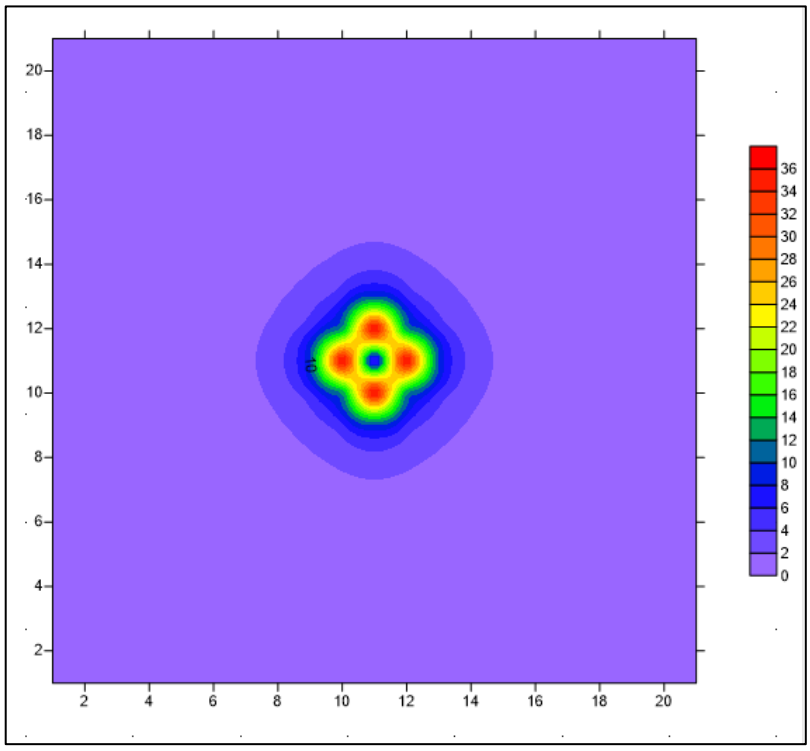


**Figure 15 - Semi-Asymptotic Sensitivity Model for Frequency 1.**

In the next chapter, I describe the application of this approach to a hydraulically fractured well where the goal is to estimate the hydraulic fracture permeabilities.

# Chapter 4: Application of Semi-Analytic Approach to Estimating Hydraulic Fracture Properties

In the previous chapter, I described the semi-analytic sensitivity computation and demonstrated the excellent correspondence between numerical sensitivities and the semi-analytic sensitivities using a synthetic case study.

In this chapter, I describe the application of the approach to estimate hydraulic fracture permeabilities from bottomhole pressure data using synthetic oil and gas reservoir case studies as well as a field case study based on a well from the Eagle Ford shale play.

## 4.1 Application to Synthetic Case Studies

The synthetic case study used to demonstrate the low frequency asymptotic approach to estimation of hydraulic fracture properties. The fractured model is defined on a 21x21x1 mesh with the producing well located in the middle of the reservoir. The reservoir has a permeability of 8.12 millidarcies and porosity of 10%. A single bi-wing hydraulic fractures characterized by 21 gridcells with a permeability of 1000 millidarcies intersects the well as seen in **Fig. 16.** The well is constrained to produce at a rate of 35 bbl/D. The procedure described in Chapter 4 is employed for the sensitivity calculations.

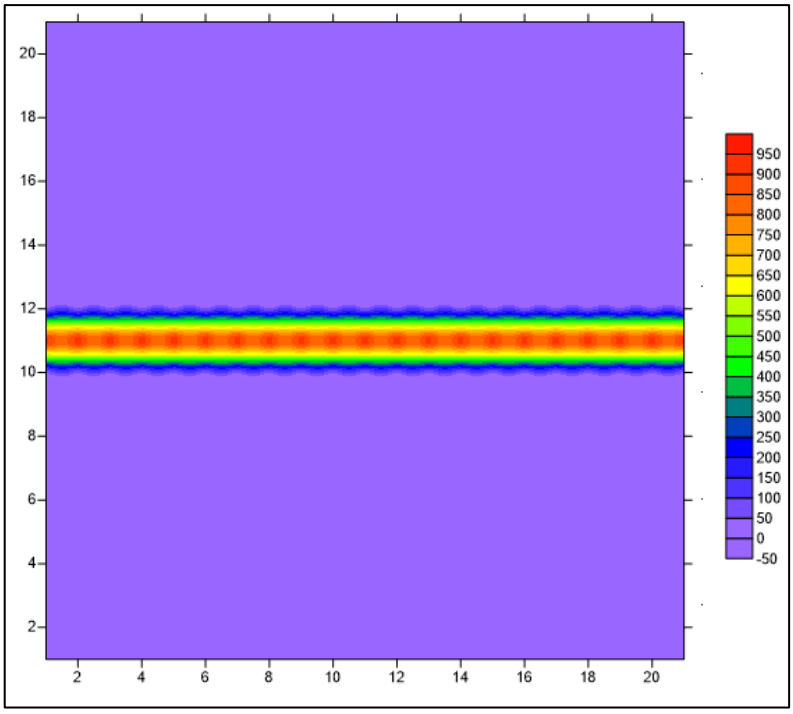


**Figure 16 - Initial permeability pattern of the synthetic reservoir model.**

### 4.1.1 Synthetic Oil Reservoir Case Study

As mentioned above, the oil reservoir has a formation permeability of 8.12 md and hydraulic fracture permeability of 1000 md. The reservoirs properties are listed in **Table 1.**

Table 1 - Reservoir Properties for Synthetic Oil Reservoir

| | | |
|---|---|---|
| Initial Reservoir Pressure | 3000 | Psi |
| Depth | 1000 | ft |
| Net Thickness | 37 | ft |
| Initial Water Saturation | 22.1 | % |
| Reservoir Formation Porosity | 10 | % |
| Reservoir Formation Permeability | 8.12 | md |
| Initial Solution Gas-Oil Ratio | 1.27 | Mscf/stb |

I use these values of permeabilities to generate bottomhole pressure data which will serve as reference or true data for this synthetic case study. My initial guess for the fracture permeability is 100 md as shown in **Fig. 17**. I attempt to use a starting (or prior) model with a background permeability of 8.12 md and a fracture permeability of 100 md to generate model-predicted bottomhole pressures.

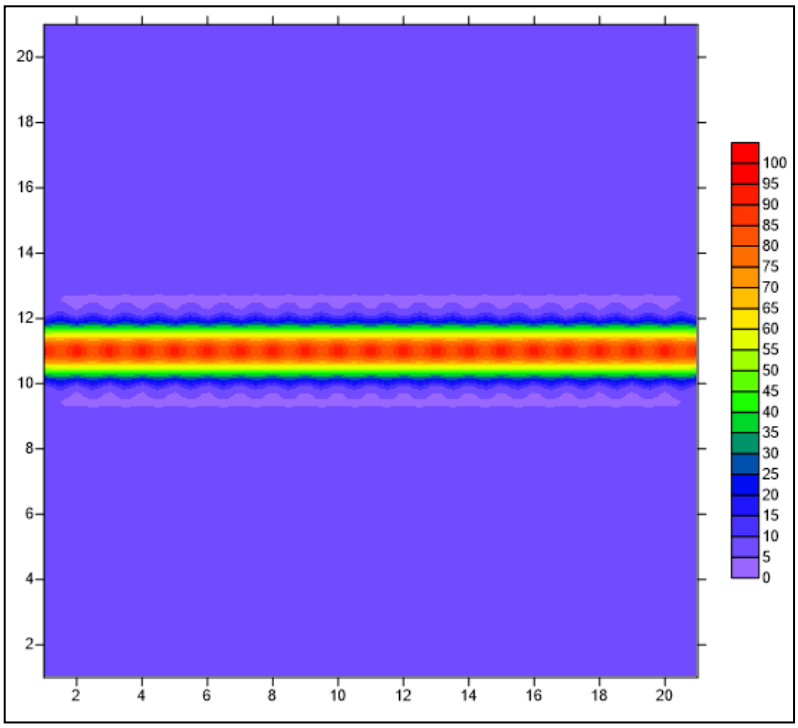


**Figure 17 - The permeability pattern for the initial guess for the fracture permeability**

The observed (or reference) and predicted values for the pressure variations are shown in **Fig. 18.** It can be seen that the trend exhibited by the observed and the predicted pressure values are somewhat similar. However, the bottomhole pressure data from Fig. 18 is then Fourier transformed and the frequency-domain misfit is computed.

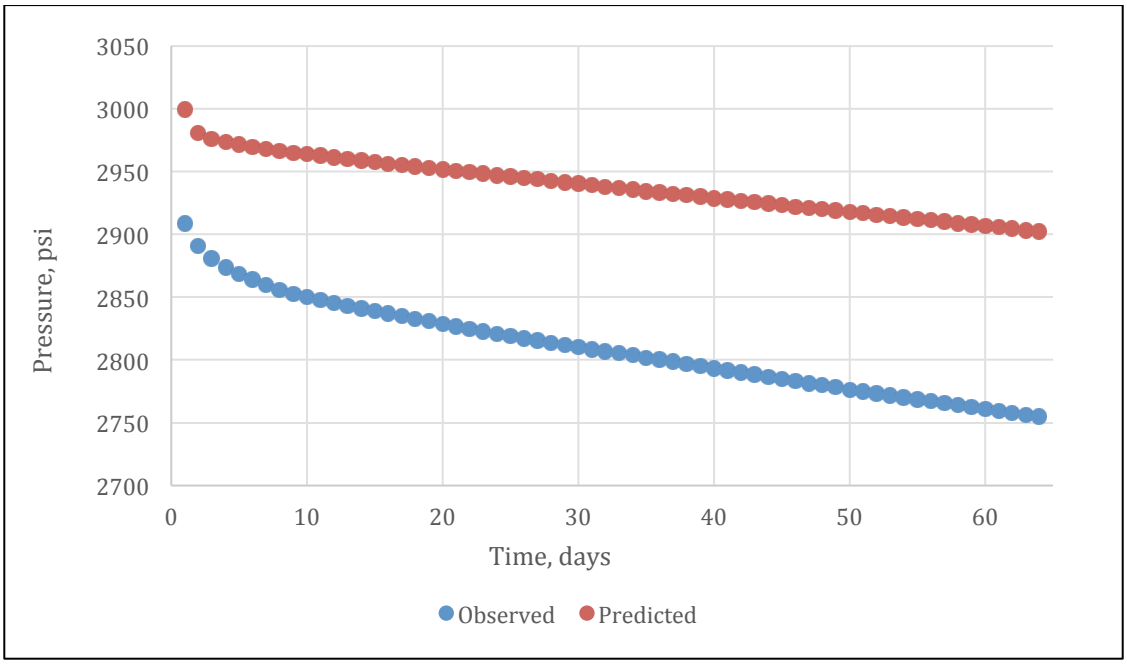


**Figure 18 - Pressure values for predicted and observed states.**

For the initial guess of 100 md, I compute the semi-analytic sensitivities as shown in **Fig. 19**. The numerical sensitivities for this model is shown in **Fig. 20**. Although there are differences between the two figures, it is important to note that the high sensitivity regions in both figures show excellent correspondence, again proving the validity of the semi-analytic sensitivity approach. The differences in sensitivity magnitudes between the numerical and the analytical method is a result of calculation rescaling. One important factor to note is the total time required for the sensitivity calculations. The total time required for the numerical sensitivity method is approximately 40 minutes of running time. However, implementing the semi-asymptotic sensitivity calculation requires only a few seconds of running time and therefore can easily be extended to even larger field-scale studies.

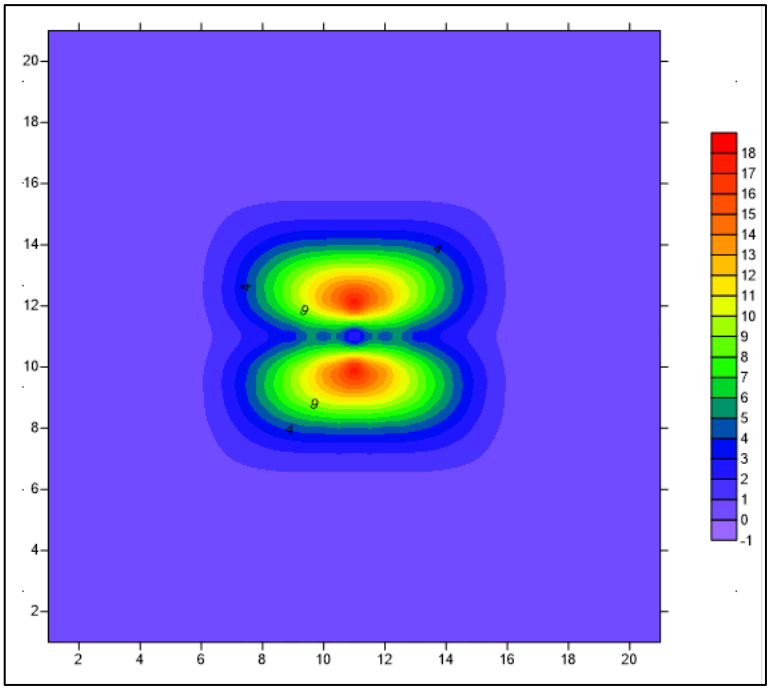


**Figure 19 - Semi-Asymptotic Sensitivities for the oil case model.**

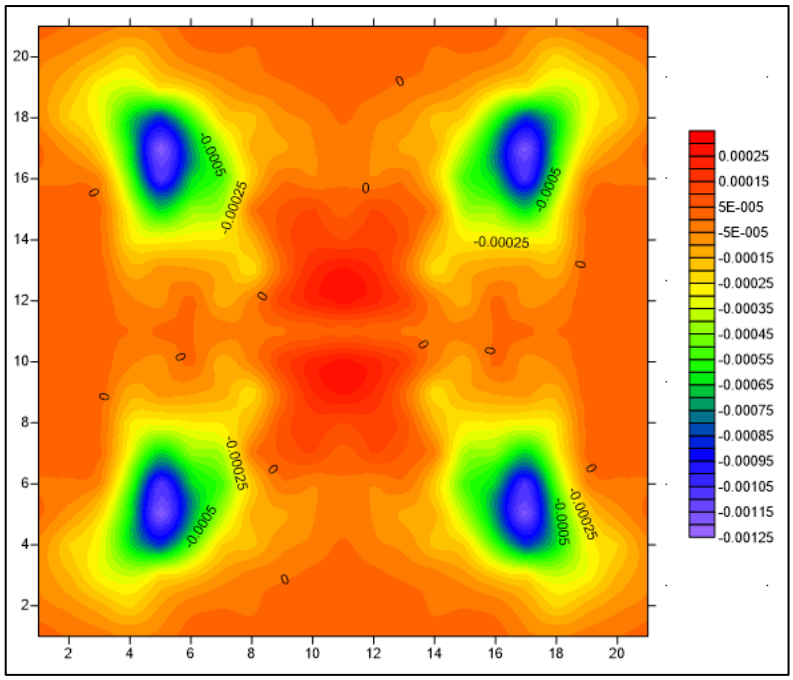


**Figure 20 - Numerical Sensitivities for the oil case model.**

These sensitivities are then utilized in an inverse approach (Vasco and Karasaki 2006) to generate updates to the permeability field in the first iteration. The pressure data misfit and sensitivities are then computed again

using the new permeability field and updated in a second iteration. This process can be continued over several iterations till the bottomhole pressure data misfit is acceptable. At that point, the model-predicted bottomhole pressure is reconciled with observations and the fracture permeabilities are then output.

The pressure misfit over 10 additional iterations is shown in **Fig. 21.** The total misfit values are calculated for pressure perturbations in both time and frequency domains and the misfit is seen to reduce considerably over 10 iterations.

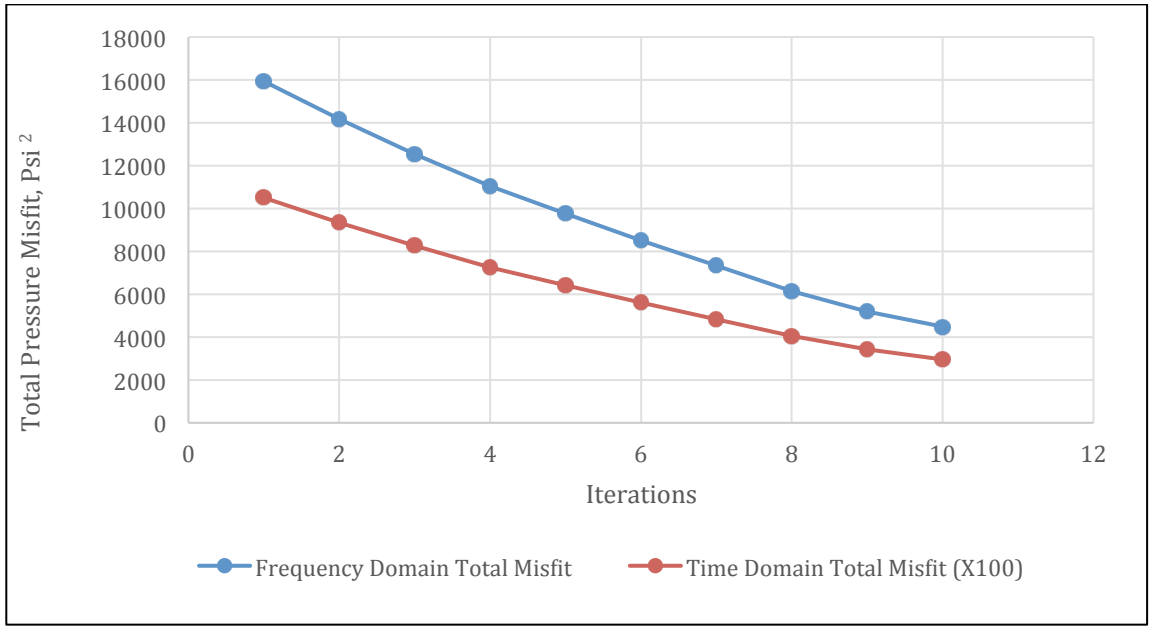


**Figure 21 - Total misfit calculated in frequency and time domains for 10 iterations.**

The final bottomhole pressures compared to observed pressures are shown in **Fig. 22**. Comparing Figs. 18 and 22, one can noticed the difference between the two bottomhole pressures has reduced significantly.

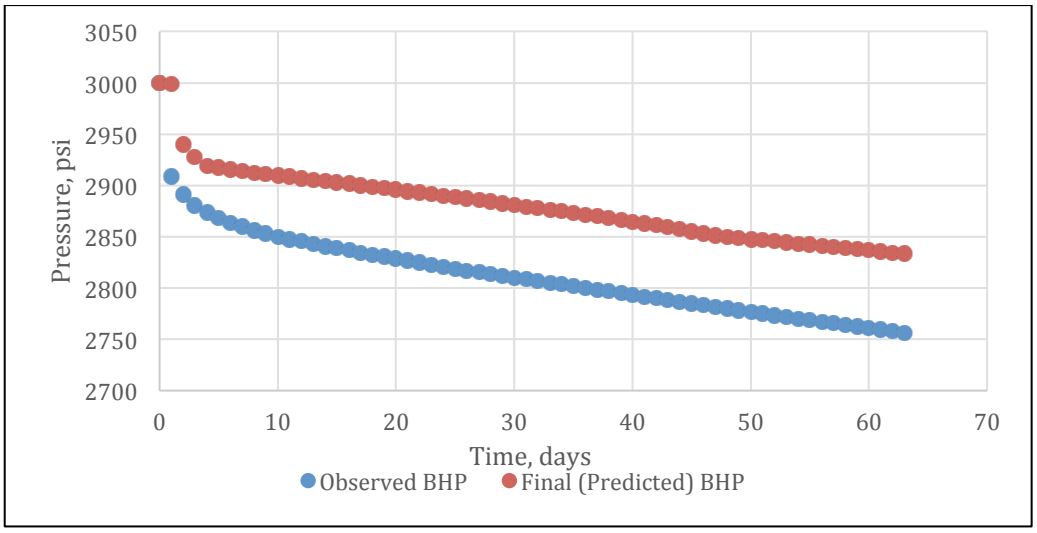


**Figure 22 - The final bottomhole pressures versus the observed bottomhole pressures.**

The final result of the permeability field is shown in **Fig. 23**. The permeability does not change substantially from the prior model. The entire solution for this problem only required a few seconds of computation time. This is a key advantage of the proposed approach over the use of numerical sensitivities that will require 442 simulation runs for each iteration.

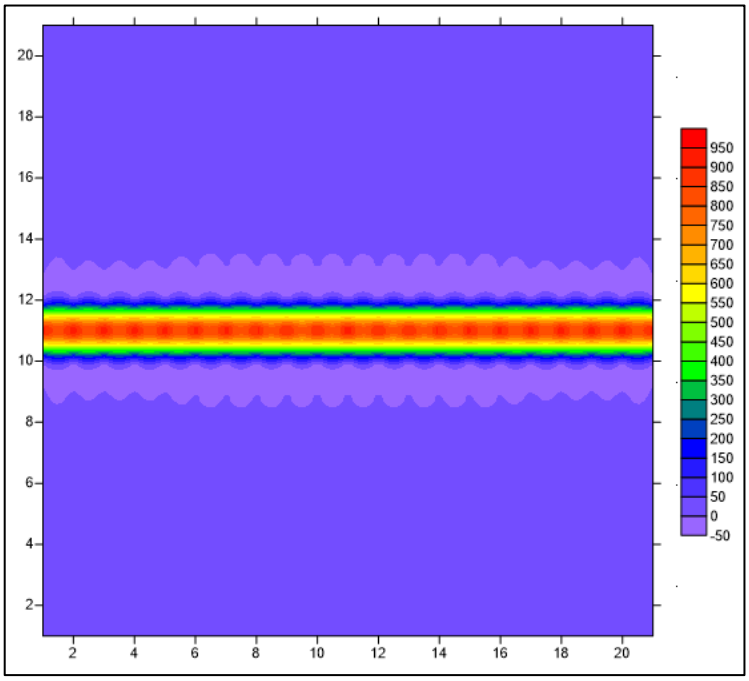


**Figure 23 - The final result of permeability estimation through pressure variations Inversion.**

The misfit between the initial and the final permeabilities for the ten iterations is shown in **Fig. 24.** The misfit was calculated by squaring the difference of the initial and final permeabilities. Generally, the misfit is decreasing with increasing number of iterations. This proves that the updated permeability patterns are approximately similar to the expected or the reference permeability.

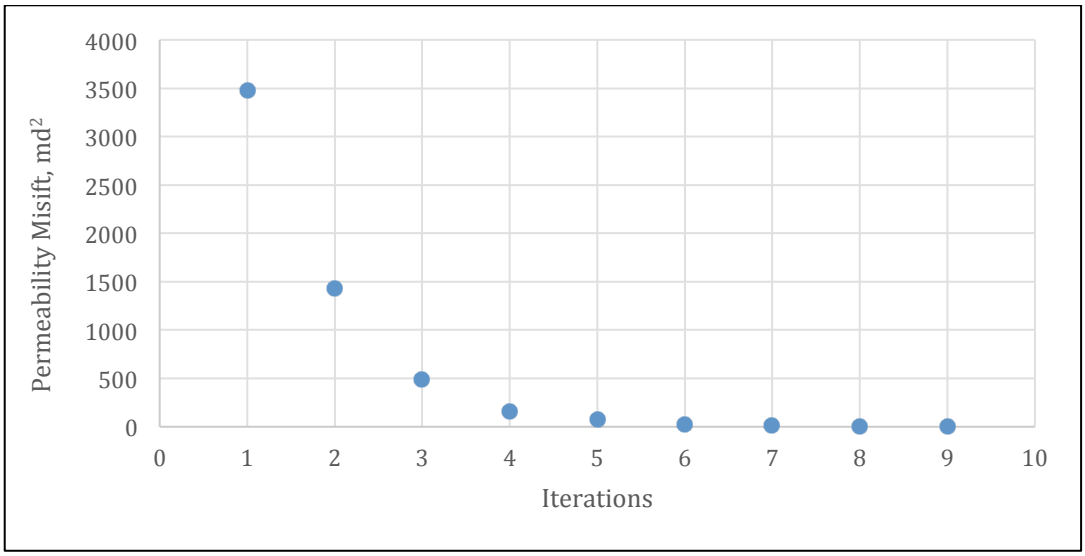


**Figure 24 - The total permeability misfit of the synthetic oil reservoir for 10 iterations.**

### 4.1.2 Synthetic Gas Reservoir Case Study

In this section, I describe the utility of the proposed approach to a dry gas reservoir. Again, the model is defined on a 21x21x1 mesh reservoir with a producing well in the middle. The formation and fracture permeabilities are 8.12md and 1000md respectively. The reservoirs properties are listed in **Table 2.**

Table 2 - Reservoir Properties for Synthetic Gas Reservoir

| | | |
|---|---|---|
| Initial Reservoir Pressure | 3000 | Psi |
| Depth | 1000 | ft |
| Net Thickness | 37 | ft |
| Initial Water Saturation | 22.1 | % |
| Reservoir Formation Porosity | 10 | % |
| Reservoir Formation Permeability | 8.12 | md |

The prior model (or initial model) has a fracture permeability of 100 md. The pressure-time plot for the predicted and observed bottomhole pressures is shown in **Fig. 25.**

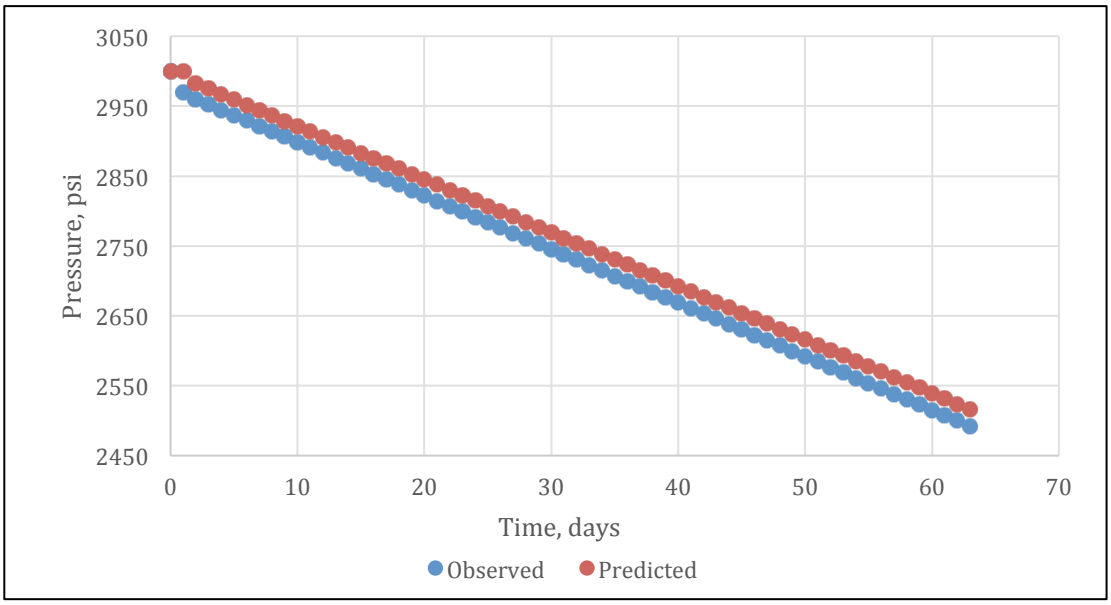


**Figure 25 - The pressure values for predicted and observed states.**

The misfit between the predicted and observed pressure values are shown in **Fig. 26** showing a decrease in the misfit over successive iterations.

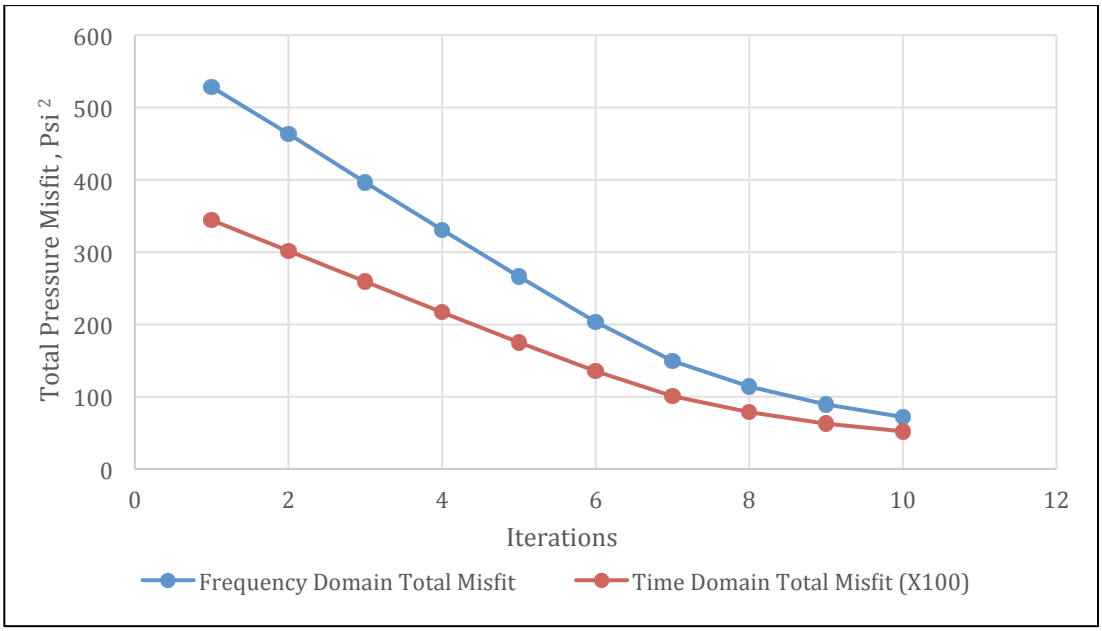


**Figure 26 - Total misfit calculated in frequency and time domains for 10 iterations.**

Eqs. 53 and 68 are used for the calculation of the semi-analytical sensitivities; results are shown in **Fig. 27.** The numerical sensitivities are shown in **Fig. 28.** The highest sensitivities are concentrated around the well and in direction of the highest permeabilities.

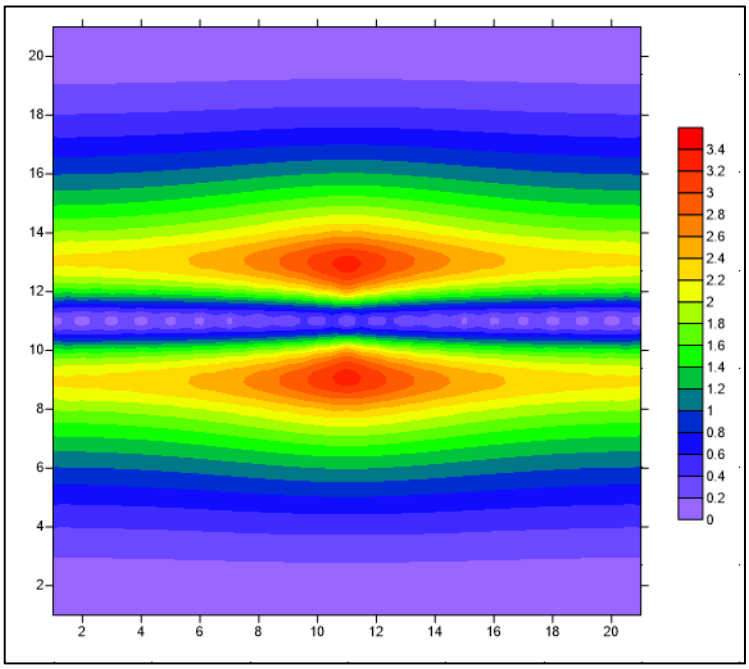


**Figure 27 -Semi-Asymptotic Sensitivities for the gas case model.**

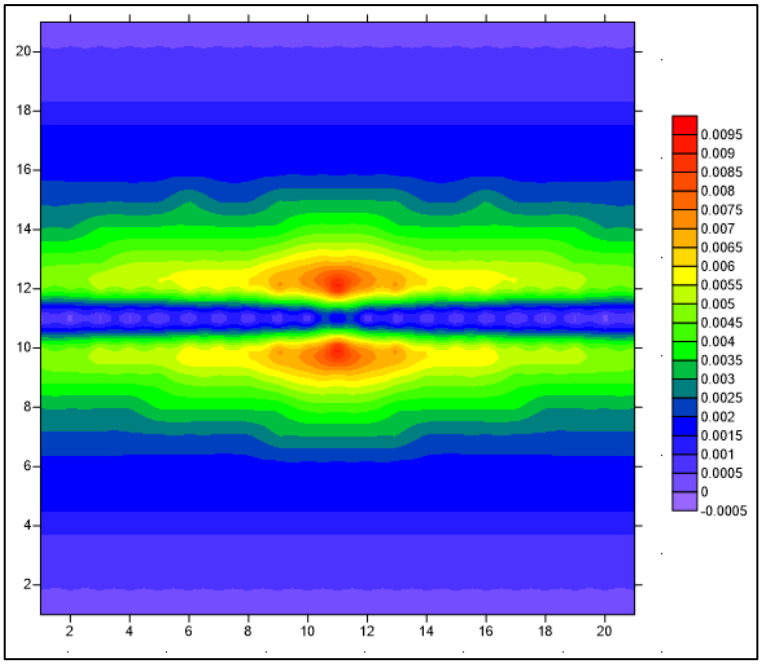


**Figure 28 -Numerical Sensitivities for the gas case model.**

The final bottomhole pressures are shown in **Fig. 29.** A comparison between the observed bottomhole and the final bottomhole pressures is also shown in Fig. 29. The difference between the two bottomhole pressures shown in Fig. 29 decreased considerably compared to the difference of Fig. 25.

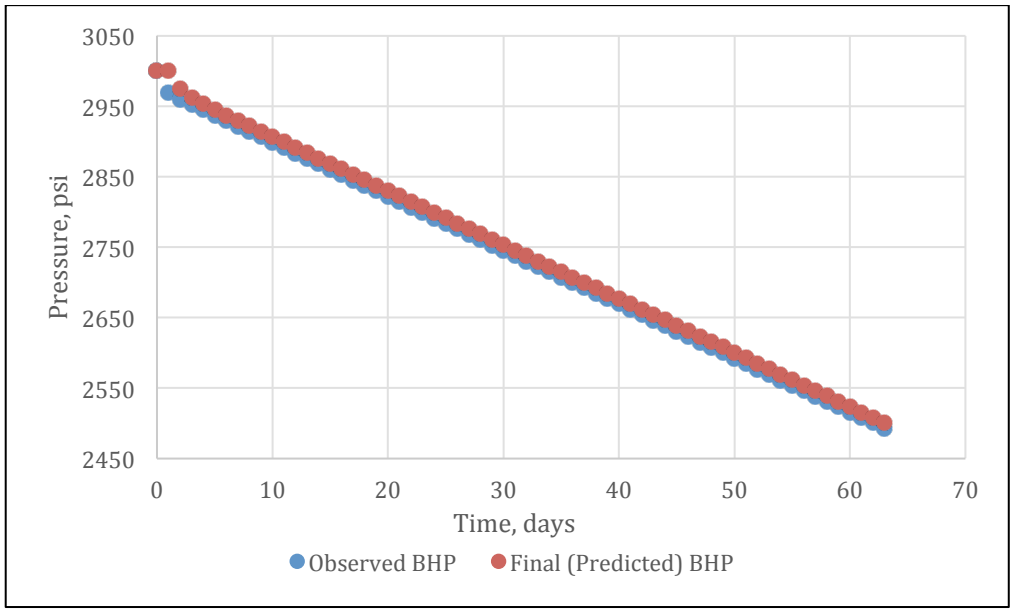


**Figure 29 - The bottomhole pressure values for final (predicted) and observed states**

Both the misfit and the sensitivities are already calculated, we are now able to update the permeability model. The reconstructed permeability of the reservoir is shown in **Fig. 30.**

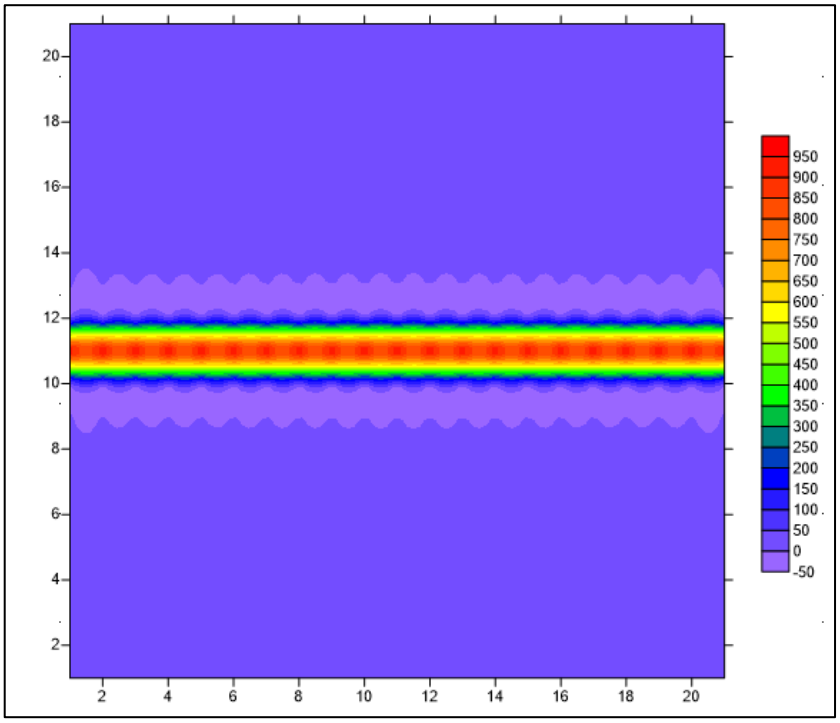


**Figure 30 - The reconstructed permeability of the synthetic gas reservoir model.**

If we were to compare reference and reconstructed permeabilities, we would be able to see that the difference is minimal. The total permeability misfit for 10 iterations is shown in **Fig. 31.** It can be noticed that the misfit is mainly decreasing with successive iterations.

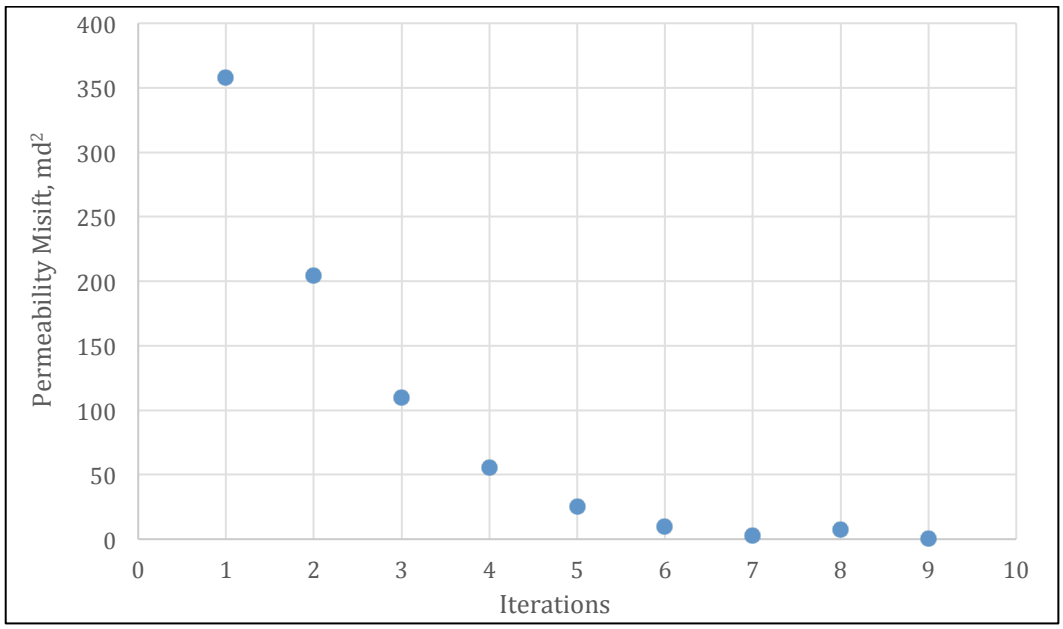


**Figure 31 - The total permeability misfit of the synthetic gas reservoir for 10 iterations.**

After demonstrating the power and utility of this approach on synthetic case studies, I now describe its application to a field study based on an Eagle Ford shale volatile oil well.

### 4.2 Eagle Ford Shale Reservoir Model

The model for the Eagle Ford volatile oil well model is defined on a 53x53x1 mesh model with one producing well. The reservoir drainage area is approximately 50 acres with a total net pay of 150 ft. The fluids of Eagle Ford formation range from dry gas to black oil (Ilk and Broussard 2012); however this model belongs to the volatile oil window of the play. The reservoir data are collected from Texas Railroad Commission (Railroad Commission of Texas 2013). In addition, the field data including the bottom-hole pressure and the oil

rates are taken from (Ilk and Broussard 2012). The reservoir and fracture properties of the Eagle Ford shale model are listen in **Table 3.**

Table 3 - Reservoir Properties of the Eagle Ford Shale Reservoir

| | | |
|---|---|---|
| Initial Reservoir Pressure | 6000 | Psi |
| Depth | 7000 | ft |
| Net Thickness | 150 | ft |
| Initial Water Saturation | 20.0 | % |
| Reservoir Formation Porosity | 9.0 | % |
| Reservoir Formation Permeability | 0.003 | md |
| Hydraulic Fracture Permeability | 1500 | md |
| Initial Solution Gas-Oil Ratio | 0.812 | Mscf/stb |

The well produces for 480 days and it encounters two shut-ins early and late in the life of the well. The formation permeability is 0.003 md while the fracture permeability is 1500md. The initial permeability pattern of the reservoir model is shown in **Fig. 32**.

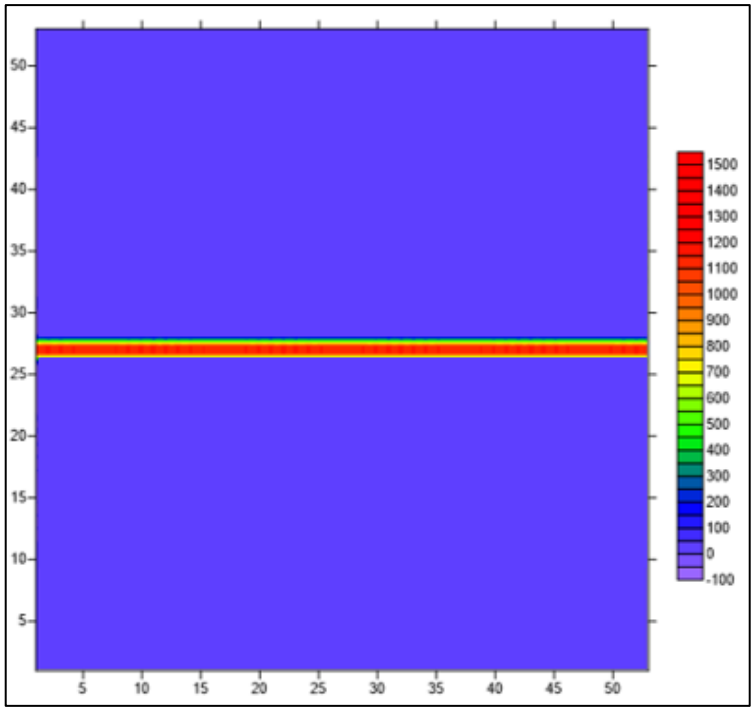


**Figure 32 - Initial permeability pattern of the Eagle Ford reservoir model.**

The observed and predicted pressure data is shown in **Fig. 33**. The PVT properties remain confidential and are not reported in this thesis. The reservoir contains fractures with permeabilities of 1500 md. A comparison between the predicted and observed pressure is shown in Fig. 33.

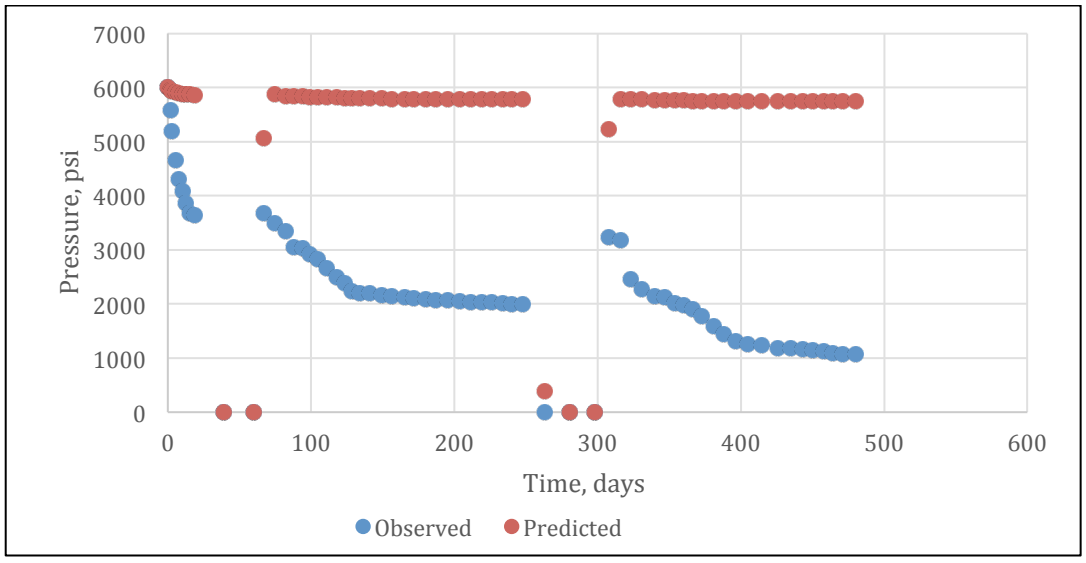


**Figure 33 - Observed and predicted pressure data.**

The pressure data misfits as a function of iteration are shown in **Fig. 34.**

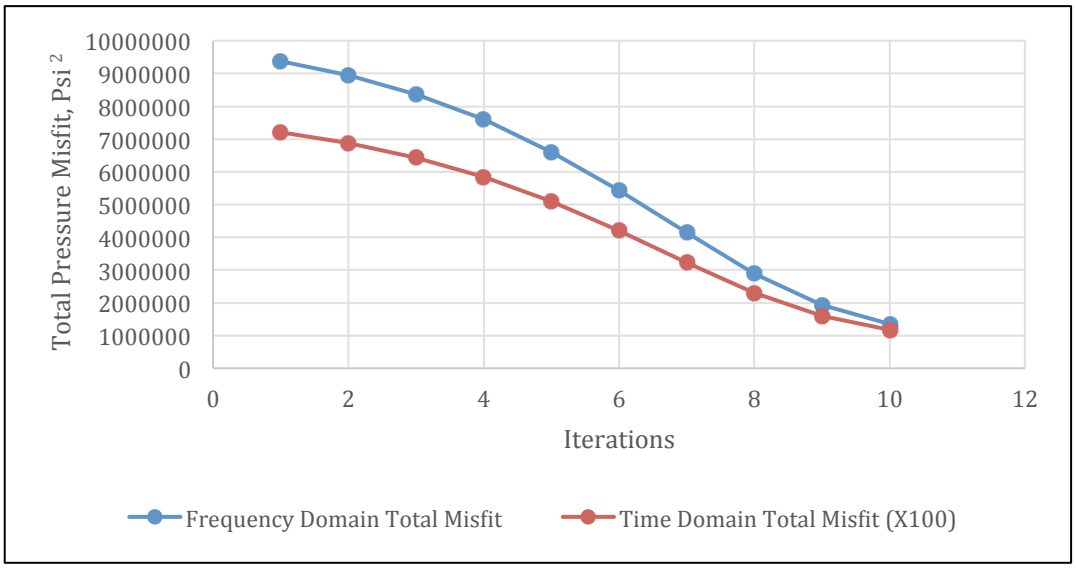


**Figure 34 - The total pressure misfit for 10 iterations. The misfit is reducing with more iterations.**

The semi-asymptotic sensitivities of the reservoir model are shown in **Fig. 35.** The large-scale sensitivity trends are analogous to those shown earlier with the synthetic case studies. In addition, the highest magnitudes of sensitivities are noticed along the hydraulic fracture and the well.

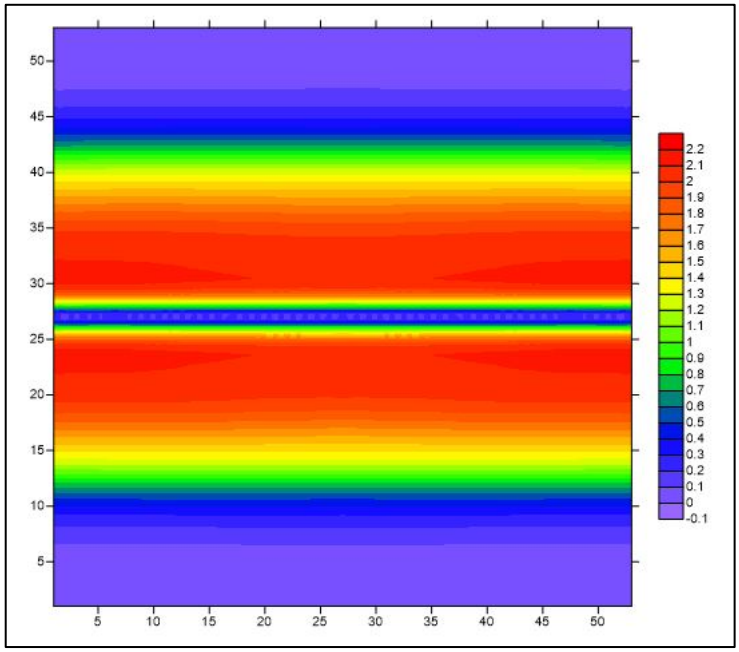


**Figure 35 - Analytical Sensitivities for the Eagle Ford reservoir model.**

The observed and final bottomhole pressure data is shown in **Fig. 36.** We can see that there is a dramatic improvement in the predicted BHP in comparison to the initial values shown in Fig. 33. Although the match cannot be considered satisfactory, this is because the model chosen for demonstration is simplistic and contains a single bi-wing hydraulic fracture. Additionally, because this well belongs to the Eagle Ford shale, there are stress sensitivities that I have not considered in my reservoir model. Nevertheless, Fig. 36 shows great improvement and if the complete physics/completion details are included, it is likely to result in a better match and a more realistic final model.

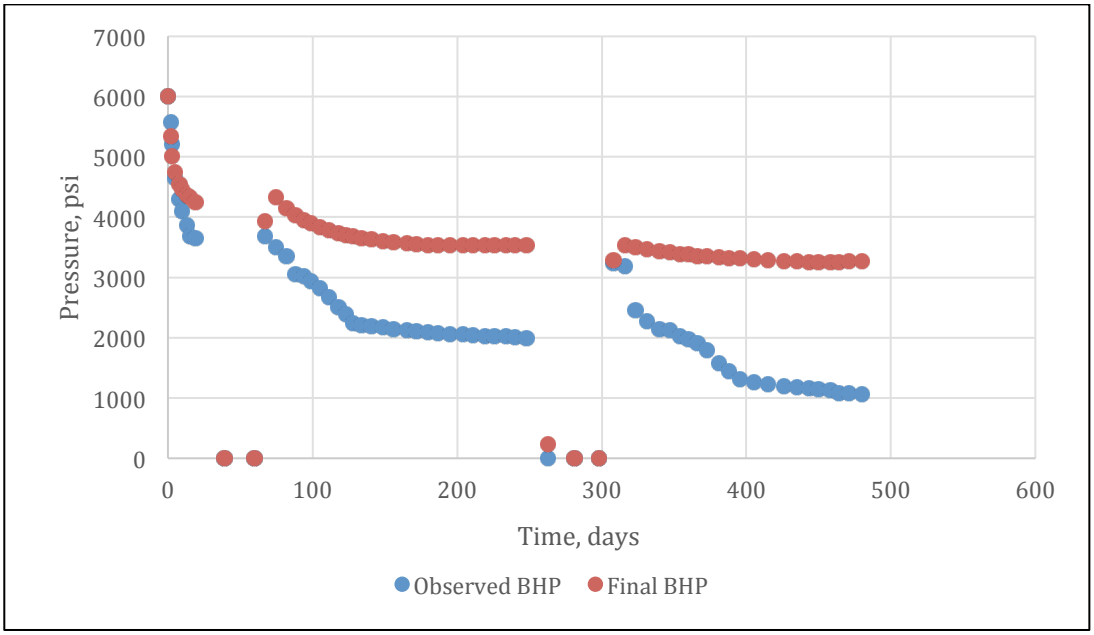


**Figure 36 - The observed and final bottomhole pressure data.**

The final estimated permeability of the reservoir model is shown in **Fig. 37**.

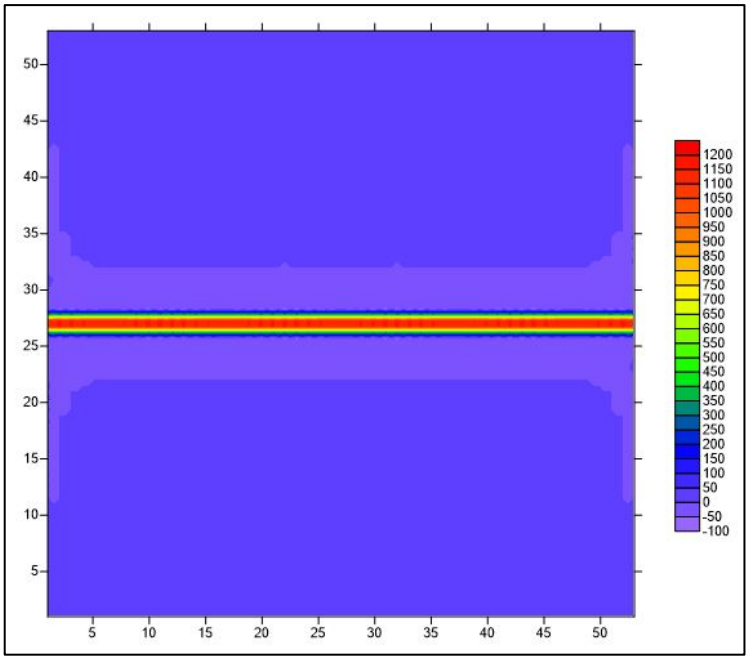


**Figure 37 - The final permeability patterns of the Eagle Ford reservoir model.**

# Chapter 5: Conclusions

A low frequency asymptotic formulation for pressure inversion was introduced to estimate hydraulic fracture properties from well pressure data. This method is shown to be promising and has several advantages over the use of decline curve analyses or pressure/rate transient analyses.

The method relies on interpreting the low frequency content of the bottomhole pressure data and therefore considerably reduces the number of observations required for estimation of formation/fracture properties. Working in the low frequency domain also makes the method robust to high frequency noise in the measurements. Model parameter sensitivity calculations relate perturbations in pressure variation to perturbations in the hydraulic fracture properties. The sensitivities computed using the proposed semi-analytic approach and the numerical sensitivities show excellent agreement, but require significantly less computational effort and time.

The power and utility of the low-frequency asymptotic approach was demonstrated on two synthetic and one field case studies. In all case studies, the inversion approach was able to reconcile model-predicted bottomhole pressures with observed values by calibrating the formation and fracture permeabilities.

## 5.1 Recommendations and Future work

In this study, for the purposes of demonstration, I restricted the case studies to a simple, bi-wing hydraulic fracture. In reality, fracture systems can be complex and can include sealed and re-activated natural fractures in addition to a more complex hydraulic fracture geometry. Additionally, several formations may be stress-sensitive and the fracture conductivity and formation permeability may be strong functions of the in-situ stresses and pore pressures. My recommendation for future work is to extend the method proposed in this thesis to such case studies with the correct physical assumptions.

# References


Aanonsen, S., Nævdal, G., Oliver, D. et al. 2009. The Ensemble Kalman Filter in Reservoir Engineering–A Review. SPE Journal **14**(3):393–412. SPE-117274-PA. http://dx.doi.org/10.2118/117274-PA.

Alzate, J., and Devegowda, D. 2013, Integration of surface seismic, microseismic, and production logs for shale gas characterization: Methodology and field application. Interpretation **1**(2): SB37–SB49.

API HF1. *Hydraulic Fracturing Operations—Well Construction and Integrity Guidelines*. 2009. Washington, DC: API.

Arps, J. 1956. Estimation of Primary Oil Reserves. Petroleum Transactions, AIME **207**(1): 182-191.

Arroyo, E., Devegowda, D. and Datta-Gupta, A. 2008. Streamline assisted ensemble Kalman filter for rapid and continuous reservoir model updating. SPE Reservoir Evaluation and Engineering **11**(6):1046–1060. SPE-104255-PA. http://dx.doi.org/10.2118/104255-PA.

Bai, M. 2015. Why are brittleness and fracability not equivalent in designing hydraulic fracturing in tight shale gas reservoirs. Petroleum **2**(1): 1-19.

Barree, R., Fisher, M., and Woodroof, R. 2002. A Practical Guide to Hydraulic Fracture Diagnostic Technologies. Presented at the SPE Annual Technical Conference and Exhibition, San Antonio, Texas, 29 September-2 October. SPE-77442-MS. http://dx.doi.org/10.2118/77442-MS.

Bennett, C., Reynolds, A., Raghavan, R., et al. 1986. Performance of Finite-Conductivity, Vertically Fractured Wells in Single-Layer Reservoirs. SPE Formation Evaluation **1**(4): 399-412. SPE-11029-PA. http://dx.doi.org/10.2118/11029-PA.

Bennet, L., Calvez, J., Sarver, D. et al. 2005. The Source for Hydraulic Fracture Characterization. Oilfield Review **17**(4): 42-57.

Blasingame, T. 2015. Reservoir Engineering Aspects of Unconventional Reservoirs. Society of Petroleum Evaluation Engineers.

Dmour, H. and Shokir, E. 2010. Pre-Post Frac Test Data Analysis for Hydraulically Fractured Vertical Tight Gas Well- Field Case Study. Petroleum Science and Technology **28**(2): 155-175.

Economides, M.J., Nolte, K.G. 2000. Reservoir Stimulation. Third edition. Wiley, New York.

Evensen, G. 2003. The Ensemble Kalman Filter: theoretical formulation and practical implementation. Ocean Dynamics **53**(4): 343.

Fisher, M.L., Heinze, J.r., Harris, C., et al. 2004. Optimizing Horizontal Completion Techniques in the Barnett Shale Using Microseismic Fracture Mapping. Presented at the SPE Annual Technical Conference and Exhibition, Houston, Texas, 26-29 September. SPE-90051-MS. http://dx.doi.org/10.2118/90051-MS.

Gradshteyn, I. S. and Ryzhik, I. M. 2014. *Table of Integrals, Series, and Products*, fourth edition. New York: Elsevier.

Gu, Y. and Oliver, D. 2007. An Iterative Ensemble Kalman Filter for Multiphase Fluid Flow Data Assimilation. SPE Journal **12**(4): 438-446. SPE-108438-PA. http://dx.doi.org/10.2118/108438-PA.

Hubbert, M. and Willis, D. 1957. Mechanics of Hydraulic Fracturing. Petroleum Transactions, AIME **210**(1): 153-168.

Ilk, D. and Broussard, N. 2012. Production Analysis in the Eagle Ford Shale -- Best Practices for Diagnostic Interpretations, Analysis, and Modeling. Presented at the SPE Annual Technical Conference and Exhibition, San Antonio, Texas, 8-10 October. SPE-160076-MS. http://dx.doi.org/10.2118/160076-MS.

Jarvie, D., Hill, R., Ruble, T., et al. 2007. Unconventional shale-gas systems: The Mississippian Barnett Shale of North-Central Texas as one model for thermogenic shale-gas assessment. American Association of Petroleum Geologists Bulletin **91**(4): 475–499.

Jia, A., He, D., and Jia, C. 2012. Earth Sciences. In *Advances and Challenges of Reservoir Characterization: A Review of the Current State-of-the-Art*, Earth Sciences, ed. I. Ahmad Dar, Chap. 9, 207-224. InTech.

Khan, M. and Callard, J. 2010. Reservoir Management in Unconventional Reservoirs. Presented at the SPE Hydrocarbon Economics and Evaluation Symposium, Dallas, Texas, 8-9 March. SPE-130146-MS.

http://dx.doi.org/10.2118/130146-MS.

Lee, D., Bratton, T., and Birchwood, R. 2004. Leak-Off Test Interpretation and Modeling with Application to Geomechanics. Presented at the 6th North America Rock Mechanics Symposium, Houston, Texas, 5- 9 June. ARMA-04-547.

Lewis, G. and Perry, K. 2011. R&D Areas Key to Improving Fracturing. Aogr, December 2011, http://www.aogr.com /magazine/ editors-choice /rd-areas-key-to-improving-fracturing/text/javascript (accessed 20 July 2016).

Mayerhofer M., Lolon E., Warpinski, N., et al. 2008. What is Stimulated Rock Volume?. Presented at the SPE Shale Gas Production Conference, Fort Worth, Texas, 16-18 November. SPE-119890-MS http://dx.doi.org/10.2118/119890-MS.

Nolen-Hoeksema, R. 2013. Elements of Hydraulic Fracturing. Oilfield Review **25**(4): 51-52.

Ozkan, E., Raghavan, R., and Joshi, S.D. 1987. Horizontal Well Pressure Analysis. Presented at SPE California Regional Meeting, Ventura, California, 8-10 April. SPE-16378-MS. http://dx.doi.org/10.2118/16378-MS.

Peaceman, D.W. 1977. Fundamentals of numerical reservoir simulation. New York: Elsevier Scientific pub.

Pearson, C. 2001. Dimensionless Fracture Conductivity: Better Input Values Make Better Wells. Journal of Petroleum Technology **53**(1): 59–63. SPE-60184-JPT. http://dx.doi.org/10.2118/60184-JPT.

Penny, G., Conway, M., and Lee, W. 1985. Control and Modeling of Fluid Leakoff During Hydraulic Fracturing. Journal of Petroleum Technology **37**(6): 1071-1081. SPE-12486-PA. http://dx.doi.org/10.2118/12486-PA.

Perez, R., and Marfurt, K. 2015. Identification of brittle/ductile areas in unconventional reservoirs using seismic and microseismic data: Application to the Barnett Shale. Interpretation **3**(4): T233-T243.

Rahim, Z, and Holditch, S. 1992. The Effects of Mechanical Properties and Selection of Completion Interval Upon the Created and Propped Fracture Dimensions in Layered Reservoirs. Presented at the SPE Rocky

Mountain Regional Meeting, Casper, Wyoming, 18- 21 May. SPE-24349-MS.
http://dx.doi.org/10.2118/24349-MS

Rahman, M. and Joarder, A. 2006. Investigating production-induced stress change at fracture tips: Implications for a novel hydraulic fracturing technique. Journal of Petroleum Science and Engineering **51** (3-4): 185–196.

Railroad Commission of Texas. 2013. Eagle Ford Information. https://www.rrc.state.tx.us/eagleford/ (accessed 25 September 2016)

Rickman, R., Mullen, M., Petre, E., et al. 2008. A Pratical Use of Shale Petrophysics for Stimulation Design Optimization: All Shale Plays Are Not Clones of the Barnet Shale. Presented at the SPE Annual Technical Conference and Exhibition, Denver, Colorodo, 21-24 September. SPE-115258-MS.
http://dx.doi.org/10.2118/115258-MS.

Rodrigues, E. and Callard, J. 2012. Permeability and Completion Efficiency Determination From Production Data In the Haynesville, Eagle Ford and Avalon Shales. Presented at the SPE Eastern Regional Meeting, Lexington, Kentucky, 3-5 October. SPE-161335-MS.
http://dx.doi.org/10.2118/161335-MS.

Simonson, E., Abou-Sayed, A., and Clifton, R. 1978. Containment of Massive Hydraulic Fractures. Society of Petroleum Engineers Journal **18**(1): 27-32. SPE-6089-PA.
http://dx.doi.org/10.2118/6089-PA.

Smith, M. and Shlyapobersky, J. 2000. Basics of Hydraulic Fracturing. In: *Reservoir Stimulations*. 5, 1-27. Malden Massachusetts: Wiley.

Valko, P., and Economides, M.J., 1995. *Hydraulic Fracture Mechanics*. Chichester, England: John Wiley and Sons.

Vasco, D. W., and K. Karasaki. 2006. Interpretation and inversion of low-frequency head observations. Water Resources Research **42**(5).

Vasco, D. W., H. Keers, and K. Karasaki. 2000. Estimation of reservoir properties using transient pressure data: An asymptotic approach. Water Resources Research **36**(12), 3447–3465.

Veatch Jr., R. and Moschovidis, Z. 1986. An Overview of Recent Advances in Hydraulic Fracturing Technology. Presented at the International

Meeting on Petroleum Engineering, Beijing, China, 17-20 March. SPE-14085-MS.
http://dx.doi.org/10.2118/14085-MS.

Virieux, J., Flores-Luna, C., and Gibert, D. 1994. Asymptotic theory for diffusive electromagnetic imaging. Geophysical Journal International **119** (3): 857-868.

Warpinski, N.R., Schmidt, R.A., and Northrop, D.A. 1982. In Situ Stresses: The Predominant Influence on Hydraulic Fracture Containment. Journal of Petroleum Technology 34(3): 653– 664. SPE-8932-PA.
http://dx.doi.org/10.2118/8932-PA.

Wattenbarger, R.A., El-Banbi, A.H., Villegas, M.E., et al. 1998. Production Analysis of Linear Flow into Fractured Tight Gas Wells. Presented at Rocky Mountain Regional/Low-Permeability Reservoirs Symposium, Denver, Colorado, 5–8 April. SPE-39931-MS.
http://dx.doi.org/10.2118/39931-MS.

Zimmer, U. 2011. Calculating Stimulated Reservoir Volume (SRV) with Consideration of Uncertainties in Microseismic-Event Locations. Presented at the Canadian Unconventional Resources Conference, Alberta, Canada, 15-17 November. SPE-148610-MS.
http://dx.doi.org/10.2118/148610-MS.

# Appendices

## Appendix A: Nomenclature

B= Oil formation volume factor, RB/STB
$c$= Isothermal Compressibility, $psi^{-1}$
$c_t$= Total compressibility, $psi^{-1}$
$C_{fD}$= Dimensionless Fracture Conductivity
$D_i$= Initial decline rate, $1/day$
$g$ =Gravity, $ft/sec^2$
$G$= Green's Function
$G_P$= Cumulative gas production, Mcf
$h$= Thickness, ft
$k$= Formation Permeability, md
$k^b$= Background Permeability, md
$k_f$ = Permeability in the Fracture, md
K= Hydraulic Permeability, md
$K_n$= Effective permeability for the nonwetting phase, md
$k_{rn}$ = Relative permeability for the nonwetting phase
$k_{rw}$ = Relative permeability for the wetting phase
$K_w$= Effective permeability for the wetting phase, md
$m(p)$= Real gas pseudo pressure, psi/cp
$p_i$= Initial pressure, psi
$p_n$= Pressure of the nonwetting phase, psi
$p_w$= Pressure of the wetting phase, psi
$p_{wf}$= Bottomhole flowing pressure, psi
$P$= Pressure Variations, psi
$\hat{P}$= Fourier Transform of Pressure Variations, psi
q = Flow rate, STB/D
$q_D$= Dimensionless flow rate
$Q_D$= Dimensionless cumulative production
$S$= Saturation, %
$S_n$= Saturation of the nonwetting phase, %
$S_w$= Saturation of the wetting phase, %
$t$= Time, secs
T= Reservoir temperature, R
$V$= Volume, $ft^3$
$w$ = Fracture Width, ft
$x_f$= Fracture Half-Length, ft
$x_s$= Source Point, ft
$y_e$ = Distance from fracture to outer boundary, ft
α= Phase
$\lambda_n$= Mobility of the nonwetting phase, md/cp
$\lambda_t$= Total Mobility, md/cp

$\lambda_w$= Mobility of the wetting phase, md/cp
μ= Viscosity, cp
$\mu_n$ = Viscosity of the nonwetting phase, cp
$\mu_w$ = Viscosity of the wetting phase, cp
$\rho$= Density, lb/ft$^3$
$\rho_n$= Density of the nonwetting phase, lb/ft$^3$
$\rho_w$= Density of the wetting phase, lb/ft$^3$
$\vec{v}$= Velocity, ft/sec
$\vec{v}_n$= Superficial velocity of the nonwetting phase, ft/sec
$\vec{v}_w$= Superficial velocity of the wetting phase, ft/sec
$\phi$= Porosity, p.u. (%)
$\omega$= Frequency, Hz
∇= Del Operator

**Appendix B: Derivation of the Pressure Equation**

The pressure equation is derived through utilizing the Mass Balance equation, Darcy's Law, and the Equation of State. The equations governing Darcy's law in a two phase flow is as follows:

$$\vec{v}_n = -\frac{Kk_{rn}}{\mu_n}(\nabla p_n + \rho_n g \nabla \mathrm{D}) \quad \text{(B-1a)}$$

$$\vec{v}_w = -\frac{Kk_{rw}}{\mu_w}(\nabla p_w + \rho_w g \nabla \mathrm{D}) \quad \text{(B-1b)}$$

Where ($v$) is the superficial velocity and ($k_r$) is the relative permeability. The terms ($D$), (K), and (μ) define the parameters depth, absolute permeability, and viscosity, respectively. In addition, ($g$) is the gravitational acceleration and ($\rho$) is the density. The Material Balance equations for the wetting and nonwetting phases are defined below:

$$\nabla \cdot (\alpha \rho_n \vec{v}_n) + \alpha q_n = -\alpha \frac{\partial(\phi \rho_n S_n)}{\partial t} \quad \text{(B-2a)}$$

$$\nabla \cdot (\alpha \rho_w \vec{v}_w) + \alpha q_w = -\alpha \frac{\partial(\phi \rho_w S_w)}{\partial t} \quad \text{(B-2b)}$$

The notations ($S$) and ($\phi$) denote the saturation and porosity values of the wetting and nonwetting phase, respectively. The term ($\alpha$) is a geometric factor function added to account for any number of dimensions when using the equation. The following is a description of the geometric function as noted by Peaceman (1997):

One Dimension: $\alpha(x, y, z) = A(x)$

Two Dimensions: $\alpha(x, y, z) = H(x)$

Three Dimensions: $\alpha(x, y, z) = 1$

Expanding the time derivative of the continuity equation, Eqs. B-2 above generates:

$$\nabla \cdot (\alpha \rho_n \vec{v}_n) + \alpha q_n = -\alpha \left[ \rho_n S_n \frac{\partial \phi}{\partial t} + \phi S_n \frac{d\rho_n}{dp_n} \frac{\partial p_n}{\partial t} + \phi \rho_n \frac{\partial S_n}{\partial t} \right] \quad \text{(B-3a)}$$

$$\nabla \cdot (\alpha \rho_w \vec{v}_w) + \alpha q_w = -\alpha \left[ \rho_w S_w \frac{\partial \phi}{\partial t} + \phi S_w \frac{d\rho_w}{dp_w} \frac{\partial p_w}{\partial t} + \phi \rho_w \frac{\partial S_w}{\partial t} \right] \quad \text{(B-3b)}$$

Diving Eq. B-3a by $(\alpha \rho_n)$ and Eq. B-3b by $(\alpha \rho_w)$, the following equations are produced:

$$-\frac{1}{\alpha \rho_n} \nabla \cdot (\alpha \rho_n \vec{v}_n) + \frac{q_n}{\rho_n} = S_n \frac{\partial \phi}{\partial t} + \phi S_n \frac{1}{\rho_n} \frac{d\rho_n}{dp_n} \frac{\partial p_n}{\partial t} + \phi \frac{\partial S_n}{\partial t} \quad \text{(B-4a)}$$

$$-\frac{1}{\alpha \rho_w} \nabla \cdot (\alpha \rho_w \vec{v}_w) + \frac{q_w}{\rho_w} = S_w \frac{\partial \phi}{\partial t} + \phi S_w \frac{1}{\rho_w} \frac{d\rho_w}{dp_w} \frac{\partial p_w}{\partial t} + \phi \frac{\partial S_w}{\partial t} \quad \text{(B-4b)}$$

Adding Eqs. B-4a and B-4b would produce:

$$-\frac{1}{\alpha \rho_n} \nabla \cdot (\alpha \rho_n \vec{v}_n) + \frac{q_n}{\rho_n} - \frac{1}{\alpha \rho_w} \nabla \cdot (\alpha \rho_w \vec{v}_w) + \frac{q_w}{\rho_w} = S_n \frac{\partial \phi}{\partial t} + \phi S_n \frac{1}{\rho_n} \frac{d\rho_n}{dp_n} \frac{\partial p_n}{\partial t} +$$

$$\phi \frac{\partial S_n}{\partial t} + S_w \frac{\partial \phi}{\partial t} + \phi S_w \frac{1}{\rho_w} \frac{d\rho_w}{dp_w} \frac{\partial p_w}{\partial t} + \phi \frac{\partial S_w}{\partial t} \quad \text{(B-5)}$$

The wetting and nonwetting phases are the only fluids flowing in the pores, therefore the saturations are defined by:

$$S_n + S_w = 1 \quad \text{(B-6)}$$

Utilizing Eq. B-6, the equation above, Eq. B-5 can be rewritten in a compacted form:

$$-\frac{1}{\alpha \rho_n} \nabla \cdot (\alpha \rho_n \vec{v}_n) - \frac{1}{\alpha \rho_w} \nabla \cdot (\alpha \rho_w \vec{v}_w) + Q_t = \frac{\partial \phi}{\partial t} + \phi S_n c_n \frac{\partial p_n}{\partial t} + \phi S_w c_w \frac{\partial p_w}{\partial t} \quad \text{(B-7)}$$

It can be noticed that the saturations time derivatives are no longer part of Eq. B-5. The term $(Q_t)$ is the total volumetric injection rate and is defined by:

$$Q_t = \frac{q_n}{\rho_n} + \frac{q_w}{\rho_w} \quad \text{(B-8)}$$

The coefficients ($c_n$) and ($c_w$) are the nonwetting and wetting phase compressibilities and are defined by:

$$c_n = \frac{1}{\rho_n}\frac{d\rho_n}{dp_n}$$

$$c_w = \frac{1}{\rho_w}\frac{d\rho_w}{dp_w}$$

Defining the mobilities of the nonwetting and wetting phases by:

$$\lambda_n = \frac{k_{rn}}{\mu_n}$$

$$\lambda_w = \frac{k_{rw}}{\mu_w}$$

The average pressure of the two phases can be defined by:

$$p_{avg} = \frac{p_n + p_w}{2} \qquad \text{(B-9)}$$

In addition, the pressure of each phase is described below:

$$p_n = p_{avg} + \frac{p_c}{2} \qquad \text{(B-10a)}$$

$$p_w = p_{avg} - \frac{p_c}{2} \qquad \text{(B-10b)}$$

Where the term ($p_c$) is the capillary pressure of the phases. Substituting Darcy's law of Eqs. B-1 into Eq. B-7 and rearranging terms produces:

$$\left[\frac{1}{\alpha\rho_n}\nabla\cdot(\alpha\rho_n K\lambda_n) + \frac{1}{\alpha\rho_w}\nabla\cdot(\alpha\rho_w K\lambda_w)\right]\nabla p_{avg} + \left[\frac{1}{2\alpha\rho_n}\nabla\cdot(\alpha\rho_n K\lambda_n) - \frac{1}{2\alpha\rho_w}\nabla\cdot(\alpha\rho_w K\lambda_w)\right]\nabla p_c + Q_t =$$

$$\left[\left(\frac{d\phi}{dp_{avg}}\right) + \phi(S_n c_n + S_w c_w)\right]\frac{\partial p_{avg}}{\partial t} + \left[\frac{\phi(S_n c_n - S_w c_w)}{2}\right]\frac{\partial p_c}{\partial t} +$$

$$g\left[\frac{1}{\alpha\rho_n}\nabla\cdot(\alpha{\rho_n}^2 K\lambda_n) + \frac{1}{\alpha\rho_w}\nabla\cdot(\alpha{\rho_w}^2 K\lambda_w)\right]\nabla \mathrm{D} \qquad \text{(B-11)}$$

Generally, the capillary pressure is very small compared to ($p_{avg}$). The terms accompanying the depth can be considered as a modification to the source term ($Q_t$). In addition, if we were to disregard the variations of ($\alpha\rho_n$) and ($\alpha\rho_w$) with position, Eq. B-11 can be written in a more simple form as shown below:

$$\nabla \cdot (K\lambda_n + K\lambda_w)\nabla p_{avg} + Q_t \approx \phi c_t \frac{\partial p_{avg}}{\partial t} \quad \text{(B-12)}$$

The term ($c_t$) is the total compressibility which is defined by:

$$c_t = \left(\frac{1}{\phi}\right)\left(\frac{d\phi}{dp_{avg}}\right) + (S_n c_n + S_w c_w)$$

The total mobility can be defined as:

$$\lambda_t = \lambda_n + \lambda_w = \left(\frac{k_{rn}}{\mu_n} + \frac{k_{rw}}{\mu_w}\right)$$

In addition, defining the coefficient (C) as:

$$C = \phi c_t = \phi\left[\left(\frac{1}{\phi}\right)\left(\frac{d\phi}{dp_{avg}}\right) + (S_n c_n + S_w c_w)\right]$$

If we were to assume no source terms, the final form of Eq. B-12 defining the pressure equation can be written as:

$$\nabla(K\lambda_t) \cdot \nabla p_{avg} + K\lambda_t \nabla \cdot \nabla p_{avg} = C\frac{\partial p_{avg}}{\partial t} \quad \text{(B-13)}$$

**Appendix C: Asymptotic Solution**

The general form of the pressure equation $P(x,t)$ in the time domain is described by Eq. C-1 below

(General Form) $$\nabla(K\lambda_t)\cdot\nabla P + K\lambda_t\nabla\cdot\nabla P = C\frac{\partial p}{\partial t} \qquad \text{(C-1)}$$

In order to work in the frequency domain, Fast Fourier transform is applied to the pressure equation $P(x,t)$ through the integral defined by Eq. C-2.

(Integral Form) $$\hat{P}(x,\omega) = \int_{-\infty}^{+\infty} e^{-i\omega t}\, P(x,t)\, dt \qquad \text{(C-2)}$$

The resultant pressure equation after transformation to the frequency domain becomes

(General Form) $$\nabla(K\lambda_t)\cdot\nabla\hat{P} + K\lambda_t\nabla\cdot\nabla\hat{P} = \omega C\hat{P} \qquad \text{(C-3)}$$

Aiming to work in the low frequency domain, the series form of the pressure $\hat{P}(x,\omega)$ in the frequency domain (Virieux et al. 1994) is defined and utilized

(Series Form) $$\hat{P}(x,\omega) = \frac{e^{-\sqrt{\omega}\,\sigma(x)}}{\sqrt{\omega}} \sum_{n=0}^{\infty} P_n(x)\ \omega^n \qquad \text{(C-4)}$$

The function $\sigma(x)$ is defined as the phase and $P_n(x)$ is the amplitude of the pressure variations. It must be noted that the general form used to describe the pressure $\hat{P}(x,\omega)$ in the frequency domain (Virieux et al. 1994) is also used to describe the solution of the diffusion equation in the frequency domain as seen in Eq. C-5.

(General Form) $$\hat{P}(x,\omega) = \mathrm{w}(\mathrm{x},\omega)\frac{e^{-\sqrt{\omega}\,\sigma(x)}}{\sqrt{\omega}} \quad \text{(C-5)}$$

The expression w(x, ω) is defined in its series form as

(Series Form) $$\mathrm{w}(\mathrm{x},\omega) = \sum_{n=0}^{\infty} P_n(x)\ \omega^n \quad \text{(C-6)}$$

The equation representing the pressure variation $\hat{P}(x,\omega)$ in the low frequency domain is derived through the substitution of the Eqs. C-4 and C-5 into the frequency pressure equation defined by Eq. C-3. Note that in order to work in the low frequency domain, only the smallest magnitudes of frequency where ($\omega \ll 1$) were used. Therefore, the pressure $\hat{P}(x,\omega)$ represented by Eq. C-4 is significantly controlled by the first few terms. Accordingly, the final form of Eq. C-4 that can be used to adequately represent the pressure variations in the low frequency domain is described by Eq. C-7 below.

$$\hat{P}(x,\omega) = \frac{e^{-\sqrt{\omega}\,\sigma(x)}}{\sqrt{\omega}}\ P_0(x) \quad \text{(C-7)}$$

In order to calculate the low frequency pressure variations for a given model, the expressions $P_0(x)$ and $\sigma(x)$ must be known. If the series form of Eq. C-4 is substituted into Eq. C-3, the solution generated will simply be an infinite sum of expressions of various orders of $\sqrt{\omega}$. This occurs due to the significant dependency of the series expression w(x, ω) on the powers of term $\sqrt{\omega}$. As a result, only the terms of the lowest frequency ($\sqrt{\omega}$) are considered.

For simplicity purposes, Eq. C-5 will be used in the substitution instead of Eq. C-4. Generating the final solutions by substituting Eq. C-5 into Eq. C-3, requires the use of the Del operator and its identities. In this study, the Del spatial derivatives defined by the gradient ($\nabla$) and the Laplacian ($\nabla \cdot \nabla$)

notations are especially used. These expressions, depending on the operator notations and function types used, can yield vector or scalar fields when multiplied with mathematical functions.

The gradient ($\nabla$) and the Laplacian ($\nabla \cdot \nabla$) of the pressure variations defined by Eq. C-5 are solved separately for accuracy and simplicity purposes. The solutions were generated by utilizing the gradient identity $\vec{\nabla}\,(fg) = f\vec{\nabla}g + g\vec{\nabla}f$ and the Laplacian identity $\vec{\nabla}^2(fg) = f\vec{\nabla}^2 g + 2\vec{\nabla}f \cdot \vec{\nabla}g + g\vec{\nabla}^2 f$. The gradient $\nabla\hat{P}(x,\omega)$ and the Laplacian $\nabla \cdot \nabla\hat{P}(x,\omega)$ of pressure are solved below.

$$\nabla\hat{P}(x,\omega) = \mathrm{w(x,\omega)}\,\nabla\frac{e^{-\sqrt{\omega}\,\sigma(x)}}{\sqrt{\omega}} + \nabla\mathrm{w(x,\omega)}\frac{e^{-\sqrt{\omega}\,\sigma(x)}}{\sqrt{\omega}}$$

$$= \frac{e^{-\sqrt{\omega}\,\sigma(x)}}{\sqrt{\omega}}\,[\nabla\mathrm{w(x,\omega)} - \sqrt{\omega}\,\nabla\sigma(x)\,\mathrm{w(x,\omega)}] \qquad \text{(C-8)}$$

$$\nabla \cdot \nabla\hat{P}(x,\omega) = \mathrm{w(x,\omega)}\,\nabla\left(\frac{e^{-\sqrt{\omega}\,\sigma(x)}}{\sqrt{\omega}}\left(-\sqrt{\omega}\,\nabla\sigma(x)\right)\right) +$$

$$2\left(\nabla\mathrm{w(x,\omega)}\,\frac{e^{-\sqrt{\omega}\,\sigma(x)}}{\sqrt{\omega}}\left(-\sqrt{\omega}\,\nabla\sigma(x)\right)\right) + \nabla \cdot \nabla\, w(x,\omega)\frac{e^{-\sqrt{\omega}\,\sigma(x)}}{\sqrt{\omega}}$$

$$= \mathrm{w(x,\omega)}\left(\frac{e^{-\sqrt{\omega}\,\sigma(x)}}{\sqrt{\omega}}\left(-\sqrt{\omega}\,\nabla \cdot \nabla\sigma(x)\right) + \sqrt{\omega}\,\nabla\sigma(x)\frac{e^{-\sqrt{\omega}\,\sigma(x)}}{\sqrt{\omega}}\;\sqrt{\omega}\,\nabla\sigma(x)\right)$$

$$+ 2\left(\nabla\mathrm{w(x,\omega)}\,\frac{e^{-\sqrt{\omega}\,\sigma(x)}}{\sqrt{\omega}}\left(-\sqrt{\omega}\,\nabla\sigma(x)\right)\right) + \nabla \cdot \nabla\, w(x,\omega)\frac{e^{-\sqrt{\omega}\,\sigma(x)}}{\sqrt{\omega}}$$

$$= \mathrm{w(x,\omega)}\frac{e^{-\sqrt{\omega}\,\sigma(x)}}{\sqrt{\omega}}\left(-\sqrt{\omega}\,\nabla\cdot\nabla\sigma(x)\right) + \mathrm{w(x,\omega)}\omega\,\nabla\sigma(x)\,\nabla\sigma(x)\frac{e^{-\sqrt{\omega}\,\sigma(x)}}{\sqrt{\omega}} +$$

$$2\left(\nabla\mathrm{w(x,\omega)}\,\frac{e^{-\sqrt{\omega}\,\sigma(x)}}{\sqrt{\omega}}\left(-\sqrt{\omega}\,\nabla\sigma(x)\right)\right) + \nabla\cdot\nabla\, w(x,\omega)\frac{e^{-\sqrt{\omega}\,\sigma(x)}}{\sqrt{\omega}}$$

$$\nabla\cdot\nabla\hat{P}(x,\omega) = \frac{e^{-\sqrt{\omega}\,\sigma(x)}}{\sqrt{\omega}}\left(\mathrm{w(x,\omega)}\omega\,\nabla\sigma(x)\,\nabla\sigma(x) - \sqrt{\omega}\,\nabla\cdot\nabla\sigma(x)\mathrm{w(x,\omega)} - 2\sqrt{\omega}\,\nabla\sigma(x)\big(\nabla\mathrm{w(x,\omega)}\big) + \nabla\cdot\nabla\, w(x,\omega)\right) \quad \text{(C-9)}$$

The final forms of the gradient $\nabla\hat{P}(x,\omega)$ and the Laplacian $\nabla\cdot\nabla\hat{P}(x,\omega)$of pressure are illustrated in Eqs. C-8 and C-9. Consequently, these equations are substituted into the pressure equation described by Eq. C-3. The resultant expression is shown below:

$$K(x)\lambda_t\frac{e^{-\sqrt{\omega}\,\sigma(x)}}{\sqrt{\omega}}\left(\mathrm{w(x,\omega)}\omega\,\nabla\sigma(x)\,\nabla\sigma(x) - \sqrt{\omega}\,\nabla\cdot\nabla\sigma(x)\mathrm{w(x,\omega)} - 2\sqrt{\omega}\,\nabla\sigma(x)\big(\nabla\mathrm{w(x,\omega)}\big) + \nabla\cdot\nabla\, w(x,\omega)\right) + \nabla K(x)\lambda_t\frac{e^{-\sqrt{\omega}\,\sigma(x)}}{\sqrt{\omega}}\left(\nabla\mathrm{w(x,\omega)} - \sqrt{\omega}\,\nabla\sigma(x)\,\mathrm{w(x,\omega)}\right) = \omega C(x)\mathrm{w(x,\omega)}\frac{e^{-\sqrt{\omega}\,\sigma(x)}}{\sqrt{\omega}} \quad \text{(C-10)}$$

In order to simplify Eq. C-10, both sides are divided by the terms $\frac{e^{-\sqrt{\omega}\,\sigma(x)}}{\sqrt{\omega}}$ and $\sqrt{\omega}$. The final form of Eq. C-3 becomes

$$K(x)\lambda_t\left(\mathrm{w(x,\omega)}\sqrt{\omega}\nabla\sigma(x)\,\nabla\sigma(x) - \nabla\cdot\nabla\sigma(x)\mathrm{w(x,\omega)} - 2\,\nabla\sigma(x)\nabla\mathrm{w(x,\omega)} + \omega^{-1/2}\nabla\cdot\nabla\, w(x,\omega)\right) + \nabla K(x)\lambda_t\left(\omega^{-1/2}\,\nabla\mathrm{w(x,\omega)} - \nabla\sigma(x)\,\mathrm{w(x,\omega)}\right) = \sqrt{\omega}\,C(x)\mathrm{w(x,\omega)} \quad \text{(C-11)}$$

As mentioned earlier, the expression $\mathrm{w(x,\omega)}$ depends greatly on different powers of the frequency $\sqrt{\omega}$. Therefore, substituting the series form of $\mathrm{w(x,\omega)}$ into Eq. C-11 will produce a sum of infinite sources. Let us recall that in

order to work in the low frequency domain, only the lowest magnitudes of $\sqrt{\omega}$ are considered. This means, we can only use the terms of magnitudes$\sqrt{\omega}^{-1}$ ,$\sqrt{\omega}^{0}$ and$\sqrt{\omega}^{1}$ as seen below.

Terms of order$\sqrt{\omega}^{-1}$

Terms with the smallest order $\sqrt{\omega}^{-1}$provide the solution for the zeroth-order amplitude of the pressure variations, $P_0(\mathrm{x})$. This indication is described in the next equations sets.

$$K(x)\lambda_t \nabla \cdot \nabla P_0(\mathrm{x}) + \nabla [K(x)\lambda_t] \cdot \nabla P_0(\mathrm{x}) = 0 \qquad \text{(C-12)}$$

The solution for the zeroth- order amplitude $P_0(\mathrm{x})$ is provided by Eq. C-12. This scalar first-order differential equation is identical to the steady state pressure equation. Also, it is independent of frequencies thus only one solution needed per well regardless what the frequency configurations might be.

Terms of order $\sqrt{\omega}^{0}$

Expressions governed by the order $\sqrt{\omega}^{0}$, the second largest frequency magnitude, are described below.

$$\mathrm{K(x)}\lambda_t\, P_0(\mathrm{x})\nabla \cdot \nabla\, \sigma(x) + \nabla\, [K(x)\lambda_t] \cdot P_0(\mathrm{x})\, \nabla\sigma(x) + 2\, \mathrm{K(x)}\lambda_t \nabla P_0(\mathrm{x}) \cdot \nabla\, \sigma(x) = 0$$

The equation above can be rewritten in a simpler form:

$$\Omega(x)\nabla \cdot \nabla\, \sigma(x) + \Upsilon(\mathrm{x}) \cdot \nabla\sigma(\mathrm{x}) = 0 \qquad \text{(C-13)}$$

Where the terms $\Omega(x)$ and $\Upsilon(\mathrm{x})$ denote the scalar and vector coefficients defined below, respectively.

$$\Omega(x) = \mathrm{K(x)}\lambda_t\, P_0(\mathrm{x})$$

$$\Upsilon(\mathrm{x}) = \nabla[K(x)\lambda_t]P_0(\mathrm{x}) + 2\, \mathrm{K(x)}\lambda_t \nabla P_0(\mathrm{x})$$

The set of equations above help solve the phase coefficient σ(x). The phase equation, described in Eq. C-13, is a linear second-order differential equation and does not contain any frequency expressions. Therefore, it needs to be solved only once, regardless of any number of frequencies present. It is important to note the equation depends on the zeroth- order amplitude $P_0$(x), the permeability K(x), and the total mobility coefficient ($\lambda_t$). In order to solve for phase coefficient σ(x), the zeroth- order amplitude $P_0$(x) must be solved first using Eq. C-12.

Terms of order $\sqrt{\omega}^{\mathbf{1}}$

Examining the terms of order $\sqrt{\omega}^{\mathbf{1}}$, the following equations are inferred. These equations provide a relationship relating the terms σ (x) , $P_0(x)$ and $P_1(x)$:

$$\nabla \cdot [K(x)\lambda_t \cdot \nabla P_1] = [C(x) - \mathrm{K(x)}\lambda_t \nabla\sigma \cdot \nabla\sigma]P_0 \qquad \text{(C-14)}$$

The equation above is used to calculate $P_1$(x) after calculating σ (x) and $P_0(x)$ from Eqs. C-12 and C-13 that were generated earlier.